Università degli Studi di Pisa

Facoltà di ingegneria

Corso di Laurea Magistrale in Ingegneria Biomedica

Numerical estimation of mechanical properties of human trabecular bone tissue: a new method based on digital image correlation

Laureando

Carolina E. Lavecchia

Relatori

Ing. Martino Pani
Prof. Ing. Giovanni Vozzi

Anno Accademico 2013/2014

Contents

Introduction

The estimation of tissue level mechanical properties of trabecular bone is still a hard task. A widely used technique is based on the combination of mathematical models, obtained through CT images, with displacements measurements registered during uni-axial compression tests. One of the main limitation of this approach is linked to the method used to measure the displacements which considers punctual acquisition for an inhomogeneous material. Moreover, the measuring instruments require the contact with the sample surface exposed to the mechanical tests, creating local artefacts which may produce significant differences between the numerical model and physical system. Recently, techniques based on the image correlation allowed the measurement of the displacements field on a surface portion during the experimental test.
This thesis develops a method to integrate the DIC measurements with the numerical models obtained through micro-CT images, in order to estimate the mechanical properties of trabecular bone tissue. An accurate registration between experimental measures and numerical model is developed and qualified through sensitivity studies on the characterizing parameters. The comparison of the displacements measured values with the foretold ones, allows to quantify the coherence between numerical model and physical model. Finally, the acquired experimental information are used to estimate the mechanical properties at the tissue level, leading to values coherent with the estimations realized with the punctual methods, assumed as reference.

Chapter 1

Bone mechanics

The skeletal system is important to the body for its different mechanic and metabolic roles. The rigidity of bone allows to keep the shape of the body, it provides protection for soft tissues and organs, and contains in the medullary cavities the bone marrow in which blood cells are produced. It furnishes leverage system for muscle-skeletal units allowing force from muscular contraction to be transmitted from one part of the body to another during the movements. Finally, bones constitute the principal mineral reservoir of ions, principally calcium, which is important in many physiological processes. In addiction, bone is a self-repairing and self-remodelling material.

In this chapter are introduced the bone biomechanics, and the principal features related to mechanical proprieties of bone tissue are presented. Firstly bone composition and trabecular bone proprieties are described, then the bone architecture and mechanical features are presented. At the end, the techniques commonly used for the mechanical characterization of trabecular tissue modulus are summarized.

1.1 Bone composition

The bone tissue is composed of 65% inorganic and 35% organic matrix, cell and water. The organic matrix consists of 90% of collagen and 10% amorphous substance, while the inorganic is composed of small crystals with shape of needles, plates and rods located within collagen fibers. The mineral is largely impure hydroxyapatite ($Ca_{10}(PO_4)_6(OH)_2$), containing constituents such as carbonate, citrate, magnesium and fluoride. Due to its combination of inorganic and organic composition, bone is a stiff but at the same time ductile material.

1.2 From cells to different bone structures

Three levels of organization of the bone tissue can be distinguished, macroscopic, microscopic and sub-microscopic. At submicroscopic level bone is composed by cells and extracellular matrix. The principal cellular elements of bone are osteoblasts, osteoclasts, osteocytes and bone lining cells. Osteoblasts are bone-forming cells that produce all the constituents of the bone matrix and partecipate in the calcification and resorption of bone. In the active state, osteoblasts are cuboidal(15 to 30μm thick), and occur as a layer of contigue cells. In the inactive state, the osteoblasts are flattened elongated cells covering quiescent bone surface and are called *resting osteoblasts* or *lining cells*. They occupy the majority of the adult bone surface. Osteoclasts, the bone-resorbing cells, are giant cells (20 to over 100 μm thick).In the active state they adhere to bone surface on dig cavities called *Howship's lacunae*. Osteoclasts and osteoblasts are developed from precursors originating in bone marrow, and their growth are linked because the osteoblast differentiation is a requisite for osteoclast development. Osteocytes represent terminally differentiated osteoblasts and function within syncytial networks to support bone structure and metabolism. Osteocytes maintain connection with each other and the bone surface through their multiple filipodial cellular processes [11]. The osteocytes are the most abundant cell type in mature bone. They are involved in bone remodelling by transmitting to other osteocytes, with fluid flow, to respond to changes in mechanical strains.

At the microscopic level bone is composed by lamellae, lacunae and canaliculi. Due to the arrangment of this microscopic structures, two different macroscopic structures can be identified: cortical bone, in which lamellae form circumferential structure, while if are arranged in longitudinal way they would form cancellous bone (see figure 1.1).

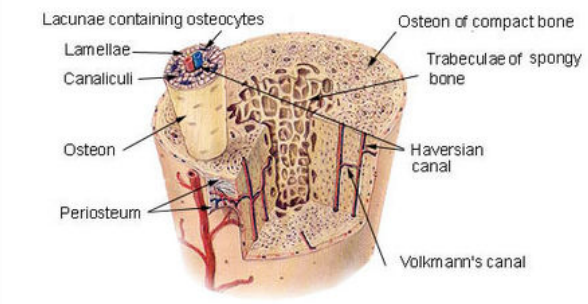

Figure 1.1: Cortical bone and spongy bone.

1.2.1 Cortical bone

Cortical bone is a dense compact structure and constitutes around the 80% of the skeleton system. In long bones, it composes the external surfaces of epipheseal regions and the diaphysis (see figure 1.2).

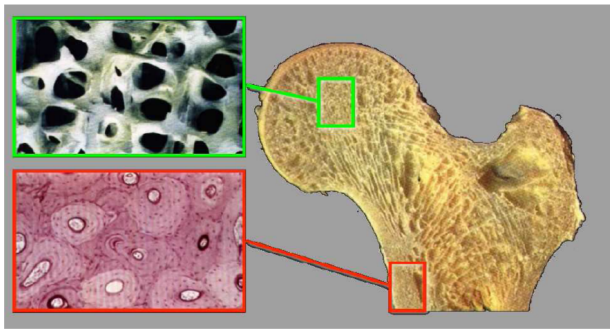

Figure 1.2: Organization of cortical (lower image) and trabecular (upper image) bone in human femour.

The thickness of cortical bone can vary between bone segments and also depending on the site of the same bone according to the mechanical stress.

1.2.2 Cancellous bone

Cancellous bone is a highly porous material, characterized by a complex internal structure and it is mainly found near the epiphysis of long bones and in vertebral bodies. Cancellous bone is formed by a tridimensional network of *trabeculae* and it forms the structural unit called hemiosteon. Trabebular orientation is not random, but it is determined by the main stress direction and the morphology can vary due to ages, pathologies and the scheleton region. In these structure cavities are filled with red-bone marrow, and are called medullary cavity [53].

1.2.3 Bone structural units

The lamellae arranged concentrically around a central canal, Haversian canal, composed the basic unit of cortical tissue, the osteon. The osteon (see figure 1.3) is formed about 20-30 lamellae and it has an external diameter of 200 to 250 μm with a lamellar circular wall of 70 to 100 μm thick. The external surface is composed of 1-2 μm thick layer of mineral collagen fibers, called cement line. Inside the structure small cavities, called lacunae, are connected each other by transverse canals called canaliculi. The network of lacune

and canaliculi, host bone cells (osteocyte) entrapped between lamellae as a result of bone formation. It has been proposed that this net acts as sensor of bone microfracture and starting a process of resorption and remodelling. Moreover, canaliculi formed a net which linked internal regions of osteon with haversian canaliculi, surface and lining cells, the marrow tissue, allowing cells to exchange nutrition and metabolites. Cortical bone is formed by

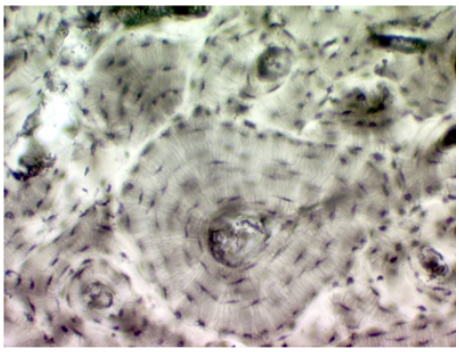

Figure 1.3: Osteon: cortical bone structural unit

three different structures: concentrical lamellae (the osteon), circumferential lamellae (a lamellar layer which forms bone external surface) and interstitial lamellae (angular framments of concentric lamellae, residuals of remodelled osteons).

In the trabecular or cancellous bone the main structural unit is the trabecular packet (see figure 1.4), also called emiosteon. The trabecular packet has cylindrical shape of 1 mm long and 50 μm thick, and as the osteon, a cement line covering trabecular packets in cancellous bone. The emiosteon is constituted by lamellar tissue aligned parallel with the trabecular surface and contained the typical lacunae due to the presence of osteocytes.

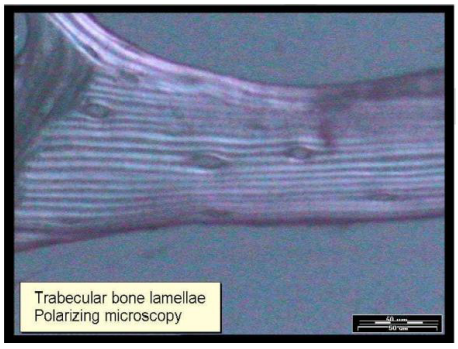

Figure 1.4: Cancellous bone structural unit

1.3 Cancellous bone proprieties

Since this thesis is focused on the assessment of the mechanical properties of the cancellous bone, a briefly introduction of the mechanical characteristic is discusses in the following paragraphs.

Trabecular composition is similar to the osteon composition in cortical tissue, but as a conseguence of the particular arrangement of trabeculae, there is a difference in bone volume fraction. In fact, cancellous bone volume fraction ranges from 5 to 60% while the cortical one is from 85 to 95%. Moreover trabecular tissue has a lower degree of mineralization and consequently lower density (1.874 g/cm^3 versus 1.914 g/cm^3). These differences are the results of the bone remodelling. The remodelling starts on the bone surface and the mineralization occurs over several months. In the cancellous bone, the surface is extended, therefore there is a large amount of new tissue which implies the presence of less mineralized and less dense tissue.

1.3.1 Architecture

Cancellous bone architecture is highly anisotropic and heterogeneous. It is important to possess solid methods for the estimation and the characterization of the trabecular structure. In fact, the variation in trabecular architecture formed the basis for the formulation of Wolff's law, which states that bone will adapt to the load under which it is placed, and links mechanical proprieties to trabecular architecture [41]. Bone architecture is characterized by several parameters such as density, trabecular orientation and thickness, which describe the structural properties and arrangement [20]. In order to study these parameters, two different methods are in use for the characterization of bone density, trabecular orientation, trabecular thickness and trabecular geometry. The first method, considered the gold standard, is the 2D histomorphometric method, while the second method is the 3D reconstruction one based on μCT scanning.

2D histomorphometric methods are based on the direct microscopical observation of specimens from histological sections. In this method, bone biopsies are embedded in a resistent material, generally PMMA (polymethylmetacrylate), which permits a mechanical sectioning into thin slice for microscope observation. Then the sections are observed through a microscope and the images are acquired by a camera. The resolution of images obtained by microscope is higher (4 μm/pixel) than microCT ones (up to 14 μm/pixel). In order to quantify the trabecular structure, the images have to be segmented distinguishing the bone and non-bone phase, once selected a grey-scale value as a limit level for bone tissue. According to American

Society of Bone and Mineral Research, the following histomorphometric parameters can be calculated to characterize each bone specimen [39, 42, 43].

- Tissue area T.Ar [mm^2]: total area of the ROI[1].
- Tissue volume TV [mm^3]: total volume of the ROI
- Bone area B.Ar [mm^2]: the sum of all pixel marked as bone.
- Bone volume BV [mm^3]: represents the bone volume occupied by bone.
- Bone perimeter B.Pm [mm]: Bone perimeter in 2D cross-section.
- Bone surface BS [mm^2]: total bone surface in 3D sample.
- Bone volume fraction BV/TV:

$$BV/TV = \frac{Bone\,Volume}{Total\,Volume} \tag{1.1}$$

- Bone surface density[mm^{-1}]:

$$BS/TV = \frac{Bone\,total\,Surface}{Total\,Volume} \tag{1.2}$$

  is the ratio of bone surface to the total volume of specimens.

The previously described parameters, called *primary indices*, are model indipendent. Moreover, there are model dependent indexes for the quantification of bone architecture, based on two opposite ideal trabecular model: the plate-model and rod-model [2]. The plate-model is the most used and this assumption is used for the calculation of the following parameters:

- Trabecular thickness [μm]:

$$Tb.Th = \frac{2}{1.199}\frac{B.Ar}{B.Pm} = \frac{1}{2}\frac{BV}{TS} \tag{1.3}$$

  it gives the thickness of trabeculae assuming a plate model.

[1] Region Of Interest: is the region of interest of the grey-scale images

[2] Rod like and plate like models are developed to classify structure that can be very different: plate like models assumed that trabecular bone could be made by parallel planes, while rod like structure assumed that trabecular bone could be organized in cylindrical interconnected structure.

- Trabecular number:

$$Tb.N = \frac{1.199}{2}\frac{B.Pm}{B.Ar} = \frac{1}{2}\frac{BS}{TV} \tag{1.4}$$

  It rapresents the number of trabecular planes per unit lenght [1/mm].

- Trabecular separation:

$$Tb.Sp = \frac{1}{Tb.N} - Tb.Th \tag{1.5}$$

  It is the distance within two plates in the plate model.

Thanks to the development of 3D-imaging techniques, it is possible to calculate structure indexes on a 3D reconstruction of the bone specimens (see figure 1.5). Three dimensional methods are based on the direct calculation

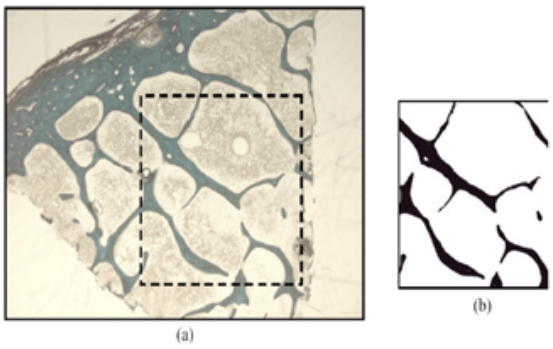

Figure 1.5: (a) Histological section of a bone sample. A central region containing only cancellous bone is selected. (b) Region of Interest (ROI): the region is binarized and the black pixel identify bone while the white identify background.

of structure indexes on a 3D reconstruction of the bone specimen without use of geometrical assumptions.

- Model independent trabecular thickness Tb.Th* [μm]: Considering a trabecular structure, trabecular thickness is calculated locally as the diameter of a sphere included within the structure (see figure 1.6). A mean value of Tb.Th* is obtained by averaging over the whole volume.

- Model Independent trabecular separation Tb.Sp* [μm]: It is calculated with the same techniques of Tb.Th*, but considering the voxel of non-bone phase.

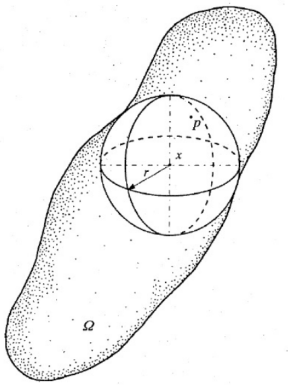

Figure 1.6: Considering a set of point which constitute a sphere, having center c and radius r, that cointain the point p and is completely included in the structure. The local thickness $\tau(p)$ is defined as the largest diameter of the sphere included in the structure.

- Mean Intercept Length MIL: it quantifies the structure interface anisotropy. The principle of this method consists of placing a linear grid with orientation ω onto a structure.

$$MIL(\omega) = \frac{L}{I(\omega)} \tag{1.6}$$

  Where I is the intersection between the grid and the bone marrow with ω orientation, and L is the line lenght of the grid. MIL varies with the orientation ω for structures with anisotropy of the bone-marrow interface, and plotting the values of MIL in a polar diagram, it approximates an ellipse for planar sections through cancellous bone (see figure 1.7)[32].

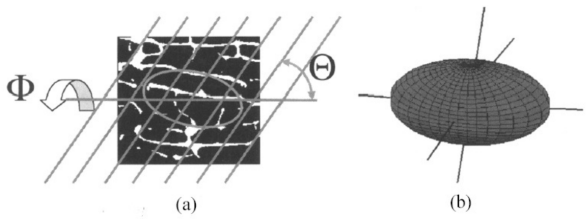

Figure 1.7: MIL method on cancellous bone.(a)A linear grid is applied on a bone section and the intersection per total length at the bone-marrow interface are counted. (b)Plotting these value in 3D, an ellipsoid is generated.

- Degree of Anisotropy (DA): it is calculated as the ratio between the major and minor axis of the ellipsoid described by the vector MIL.

$$DA = \frac{MIL_{max}}{MIL_{min}} \tag{1.7}$$

1.3.2 Apparent mechanical proprieties, asymmetry and anisotropy

Trabecular bone is a porous and interconnected material and its structure varies with ages, sites and pathologies [11]. At a scale of 4-5 mm cancellous bone can be considered a continuum material, exhibiting mean mechanical proprieties that can be referred to the specimen volume. The mechanical proprieties at the continuum level are called apparent proprieties, while the mechanical proprieties of individual trabeculae are usually referred as tissue proprieties.

Due to volume fractions, architecture, and tissue material proprieties there is a very high variation on the strenght of trabecular bone and according to *Ding et al.* [12] and *Helgason et al.*[20] the apparent modulus is affected by bone volume fraction and density. Linked to these different characteristic an important features which influences the apparent mechanical proprieties is the anisotropy. It can vary not only in different subject, but also is site-dependent and the degree of anisotropy can be calculated as in 1.7. The degree of anisotropy depends on the trabecular structure, it varies between the different bone site and with mean intercept length.

At the apparent level, in the post-elastic region trabecular bone exhibits an asymmetric behaviour between compressive and tensile tests. The figure 1.8 shows the stress-strain curves of compressive and tensile test. Looking the figure is evident the asymmetric behaviour of the trabecular bone between this two different experiments. In compression, yield stress is generally reached around 1%, while for tensile loading it is 0.78 % . In spite of this characteristics, the elastic modulus is the same in tension and compression [31][25].

1.4 Techniques in use for characterization of trabecular tissue elastic modulus

Due to the small dimension of trabecular bone, the investigation of tissue level mechanical proprieties is a hard task for the researchers. Bone mechanical proprieties vary with anatomical site, age and bone spatial arrangement

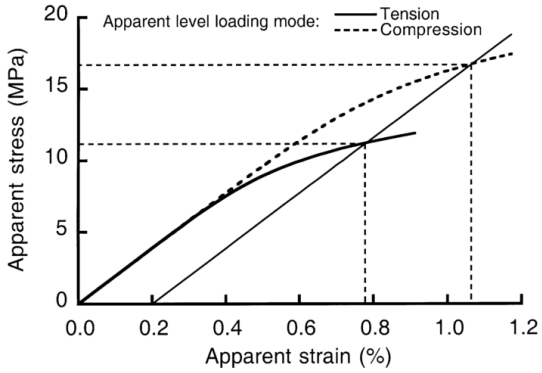

Figure 1.8: Stress-Strain curves computed by the high-resolution finite element model. These curves show the behaviour of the bone to compressive and tensile tests, where the yeld strain is calculated at 0.78% and 1.06% in tensile and compression test respectively[31].

[18]. However, recently developed experimental techniques, based on the combination of FEM modeling and experimental tests, allow to estimate the cancellous tissue modulus. Different techniques are available for evaluation of trabecular apparent modulus and the values showed in literature range from 0.7-20 GPa. Moreover, these techinique allow to evaluate the difference between cortical and cancellous bone. In fact, cancellous modulus is lower than the cortical modulus of between 10-20%. The most common techiniques for the characterization of trabecular modulus are described here.

Uniaxial Tensile Test. It is one of the most accurate methods for measuring mechanical proprieties of material and it requires an accurate preparation of the specimens. The specimen has to be relatively large and carefully machined, and due to small dimensions and the irregular shape of bone samples the utility of tensile test for cancellous bone is limited.[11]

Bending Test. In this mechanical test, bone is subjected to a combination of compression and tension. Bending can be applied to the bone in two different ways: three-point and four-point loading. Three-points method occurs when three forces acting on the specimen produce two equal moments, while four-points occurs when two couple of forces produce two equal moments. The major difference between this two methods is the construction of the actuator. Due to the irregular surface of bones, which doesn't allow the right setting of the loading, the bending test is rarely used in trabecular bone tests.

Micro and nano indentation. Micro-indentation was introduced during

the fifties, it recorded measures for trabecular bone lower than in cortical bone by 15%. In the last 20 years, new indenter were developed of 2μm in size and a depth-sensing resolution of nanometers which allow to implement repeatable measures for the bone structures. Generally, measures obtained by nano-indentation has given the higher values for bone tissue modulus[51].

Compression Testing. Compression testing of bone specimens is a common technique to test trabecular bone at the apparent level. It requires particular attention on the cut surface of the specimens. Infact, if the load surface of the bone are misaligned with respect to the actuator's platen, large stress concentration can occur. In spite of the difficulties to obtain accurate measures, the compressive test has several advantages: specimens have not to be as large as in tensile test and the fabrication of compressive specimens is not as difficult as the fabrication of tensile ones.

Micro Finite Element Analysis. In the last decades, a new approach is developed to evaluate the trabecular bone tissue proprieties. This method is based on the modelling of bone and the new micro-imaging techniques, such as micro-CT, allowing to describe the 3D microscopic structure of trabecular bone. Using a direct voxels-conversion technique the three dimensional reconstruction of bone can be converted into element (cubic or hexahedral) based micro-FEM models and it can be used to simulate mechanical tests with high accuracy and high precision [11, 1, 44, 46, 45, 36, 21, 30].

In order to evaluate the bone tissue proprieties, the same boundary conditions are imposed to mechanical tests and μFE models. Generally, uni-axial compression is applied on cubic or cylindrical bone samples, and the experimental apparent modulus (E_{app}^{exp}) is calculated from the results of mechanical test. Once chosen a tentative value for the cancellous tissue modulus of the μFEM model (E_{t}^{FEM}), the apparent modulus of the μFEM of the model (E_{app}^{FEM}) can be determined by simulation of the same boundary conditions. Hypothesizing linear elasticity, the tissue modulus is obtained as follows:

$$E_t = \frac{E_{app}^{exp}}{E_{app}^{FEM}} E_t^{FEM}$$

Nowadays this is the standard approach to calculate trabecular bone tissue properties, but due to several difficulties linked to reproduce the same boundary conditions and the lack of indipendent measures, did not use to build the FEM model, the numerical method is not validated.

In the next chapter there is an introduction on the techniques used at the Laboratory for Medical Technology of the Rizzoli Orthopaedic Institute for evaluating trabecular bone tissue mechanical proprieties.

Chapter 2

State of Art

The small dimensions of cancellous bone structural units make the investigation of tissue level mechanical proprieties an extremely hard task for the researchers. There are different techniques in use for the experimental characterization of trabecular tissue elastic modulus, such as uniaxial tensil and bending tests, ultrasonic techniques, micro-indentation and nano-indentation (for further information see chapter 1). In the last decades, experimental techniques based on the combination of mechanical tests, μCT images and FEM modeling were developed. High resolution μCT image at micro-scale allow to define a FEM model which is able to accurately describe the micro architecture of trabecular samples. Subsequently, the specimens are tested with non destructive loading tests for the determination of mechanical properties of the apparent level [1]. In order to estimate the bone tissue elastic modulus, the same boundary condition of the experimental test are applied to solve FEM model. At the date this is a standard approach for the investigation of trabecular bone tissue properties, but none verification were performed so far. Actually the experimental data are used to couple the numerical model with the physical system and none information are provided for an independent validation. Another innovative technique, that is actually under development at IOR is the combined use of mechanical test (where an extensometer measured the displacements) and the digital image correlation (DIC). This alternative technology is based on the optical detection of the displacements on the surface of the bone specimens. The combination of μFEM technique and DIC, comparing the displacement fields, would lead to different outcome.

In this chapter, all the steps which lead to DIC and FEM models are described. Particularly, a detailed description of algorithms and of each

[1] As specified in the chapter 1, apparent proprieties are referred to bone volume at a scale of 4-5 mm, while tissue proprieties are referred to the individual trabeculae.

phase of the whole procedure will be presented.

2.1 MicroCT

The imaging techniques cover an important role in different areas, from medicine to material science. The X-ray Computer Tomography has been invented in 1971 by Godfrey Housfields and it is a relatively new field of non-destructive imaging. It allows a non destructive investigation of the internal structure of objects without destroy them. This technology is based on the interaction of X-ray with matter and depending on the density of material, X-rays are more or less absorbed. X-rays, originated from a source, interact with the object and the attenuated radiation coming out from the sample is collected by the X-ray detector (in the figure 2.1 the procedure is summarized). The analysis of these projection data, by algorithms for back-

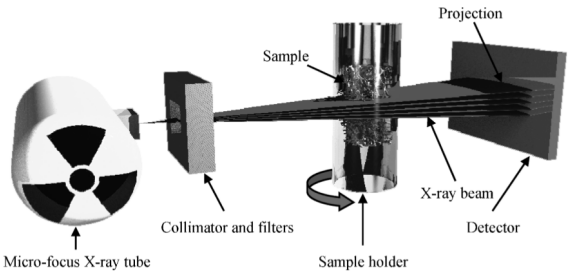

Figure 2.1: Micro-CT scan system [6].

calculation, provides a set of images corresponding to the cross section of the sample. With proper calibration of the system it is possible to convert the cross-section images (Hounsfield Units) in density images [42]. The advent of MicroCT allowed the qualitative and quantitative characterization of samples in two and three dimensions at the micro-metric range. One of the main field of application of micro-CT is the investigation of bone structure. It was developed in the late 1980s and is based on the same principle of Computer tomography. The system is composed of a microfocus tube that generates cone beam of X-rays, a rotating holder in which is mounted the specimen and a detector system to collect the images. After a proper calibration and conversion of attenuation coefficients, this leads to a cross section density image of extraordinary nominal resolution (pixel size from 4 to 30 μm for gold standard device). In the figure 2.2 is shown a grey scale cross-section of cancellous bone. The spatial resolution during a scan using a cone beam is related to the sample size, then for high resolution micro-CT scanning of

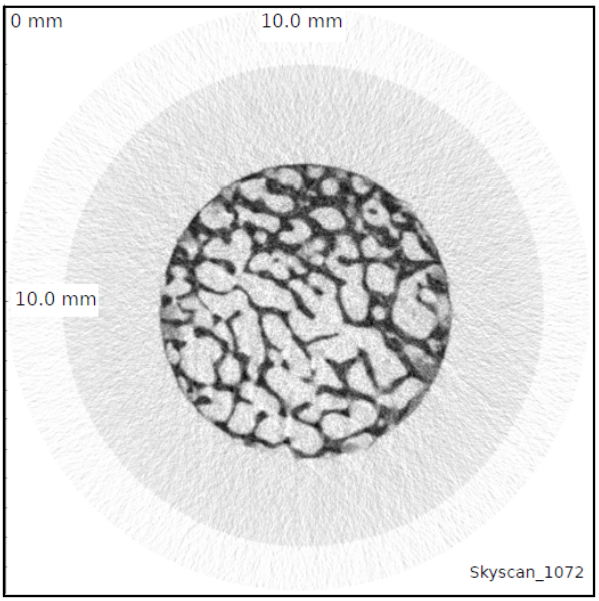

Figure 2.2: Micro-CT scan output: grey scale slice image of cancellous bone. The region of interest(ROI) is the central part of the output image.

cancellous bone, cylindrical specimens with a diameter of the order of 5 to 10 mm should be used.

2.2 From μCT to μFEM model

Such mechanical proprieties of cancellous bone depend on both the total amount of tissue and its spatial distribution. μCT imaging constitute a very effective tool to obtain an accurate description of the trabecular structure, and it may be used to realize 3D model which reflects the real micro architecture of the bone specimens.

Actually, the techniques used to estimate the mechanical properties of the cancellous bone are based on the utilization of the micro-CT to obtain information on the bone structure; then the specimens are tested with uni-axial compression and meanwhile the micro-FEM model is constructed starting from the μCT volumetric dataset; finally the model is solved considering the same boundary conditions of the experimental test. The diagram 2.3 shows the entire procedure which lead to the estimation of E_t [48, 38, 26].

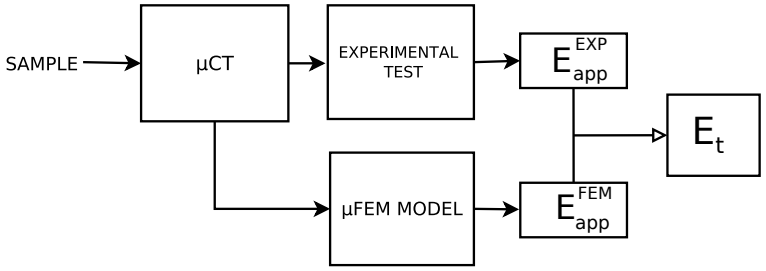

Figure 2.3: The diagram shows the procedure currently applied.

2.2.1 μCT scan

The layout used at IOR's facilities is based on the scanning of cylindrical cancellous bone specimens (height 26 mm, diameter 10 mm [17]) from biopsy of human femural head. These are scanned with Skyscan micro-CT with 0.90°rotation step over a total acquisition angle of 185°and field of view 20 x 20 mm. Obviously this field of view does not allow to scan all the specimen length, so the specimen is scanned two times and the two datasets are merged with dedicated algorithms. The data obtained from micro-CT is a stack of 1024 x 1024 pixel grey scale slice images with pixel size of 19.5 μm and z-axis step 19.5 μm, and the grey level of each pixel corresponds to the density of the matter which is scanned.

The stack of cross-section images from micro-CT is imported to a medical imaging manager software. Every image pixel is converted in a volume voxel with the same size of the native image pixel (19.5 μm) (see figure 2.4).

To reduce the total number of nodes and computational costs, this volume can be re-sampled to lower resolution: from the native pixel size of 19.5 μm to 39 μm. Then at each voxel is assigned the mean grey scale value of the native voxels. In order to obtain the morphometric parameters and the 3D model of cancellous bone structure, the grey level images have to be binarized discriminating bone and non bone. In literature different threshold methods are described for binarization of micro-CT images. In general they can be divided in two groups: global and local threshold algorithms. The global threshold technique is based on an histogram analysis (see figure 2.5) using one only threshold value on the entire stack, while the local threshold is calculated for each pixel and depends on some local statistics of the pixel neighborhood [8]. At IOR's facilities a global threshold with a grey threshold value of 117 is used, based on the comparison of binarized μ-CT images with histological observation of the same section [35].

The thresholding technique may cause the loss of trabecular connections, thus to define a 3D model, which might affect the assessment of the mechan-

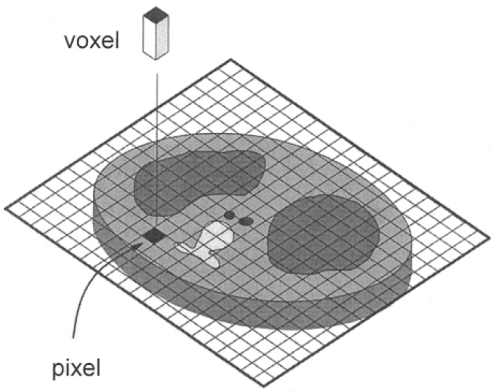

Figure 2.4: Each pixel of the reconstruction is converted in volume voxel with the same size of the native pixel. The height of the voxel corresponds to the distance between each slice given by the scanner.

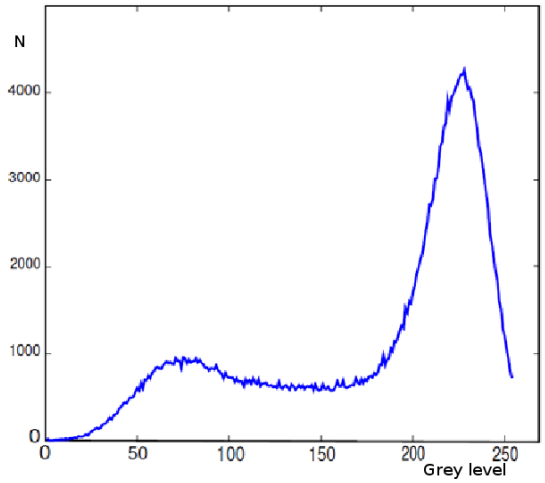

Figure 2.5: Histogram of cancellous bone cross-section attenuation coefficients where grey level are included between 0 and 256, and N is number of pixels. The grey scale is related with density of the media which is scanned. The lower density peak represents bone tissue while the higher bone marrow and the background.

ical properties based on the μCT reconstruction.

2.2.2 Experimental tests

The experimental layout of uni-axial compressive test performed at IOR's facilities is introduced here.

Figure 2.6: Experimental layout for compressive test of a cylindrical cancellous bone specimen (diameter = 10 mm, height = 26 mm)

The experimental layout (see figure 2.6) in use was developed minimizing the end-artifacts and side-artifacts in order to obtain an accurate measurement of the apparent modulus [33, 34]. A slice of 26 mm is obtained from the the donor's femoral condyles, under constant water irrigation of the sample. Subsequently cylindrical specimens (height 26 mm, diameter 10 mm) are extracted using a diamond-coated milling cutter. The extremities of the sample are cemented in 3 mm in PMMA (polymethylmethacrylate) endcups and five aluminium spheres (diameters 1 mm) are positioned in the cement in order to use them as landmarks. The specimens have to be left into Ringers solution for 24 hours and then each cylinder is scanned by micro-CT (Skyscan 1072®, BRUKER, Kontich, Belgium). The aluminium spheres allow to register the experimental test with the μCT acquisition. Before testing, the specimens are immersed in Ringers solution for another hour, thereafter they are cemented directly onto the testing machine in order to avoid the misalignment between the machine axis and the specimen. An extensometer is attached to the central part of the specimen and the gauge length L_0 is measured. Then the variation of length is measured at the end of the test, allowing the evaluation of the elastic modulus. The compressive

test is performed under displacement control at a deformation rate of 0.01 s^{-1} [34, 17, 23]. Thanks to the measure obtained with the extensometer, the elastic modulus is calculated as follow:

$$E_{app}^{EXP} = \frac{\frac{F}{A}}{\frac{\Delta L}{L_0}} \tag{2.1}$$

where F is the total applied load at the two surface, A is the nominal cross section of the bone specimens, ΔL the distance variation between the extensometer knifes before and after the measurement. During the mechanical test, load and displacement are monitored. The test is repeated four times

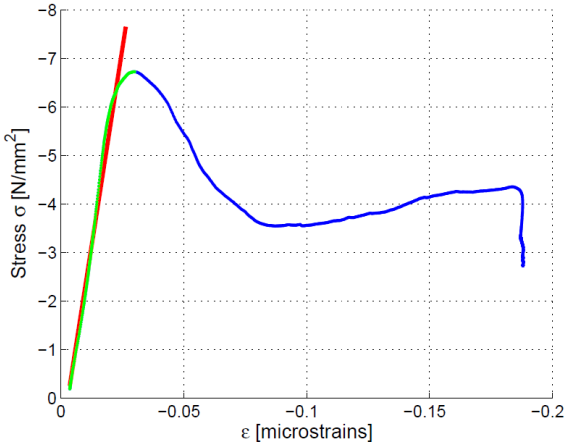

Figure 2.7: Stress-strain curve from an experimental failure compressive test. The elasticity apparent modulus is obtained from the slope of the quasi-linear loading region of the curve.

and the references of positions are constituted by the four aluminium spheres. The stiffness is calculated as the slope of the loading curve (figure 2.7) in its linear elastic region and the final elastic modulus is evaluated as the average of the modulus registered for each angular position.

Finally, a failure compressive test is performed to acquire other information on the post-elastic behaviour of the specimens.

2.2.3 Micro-FEM models

Once the volumetric bone structure is reconstructed, the micro-CT dataset is re-sampled at 39 μm to reduce the computational costs. Then 3D FEM model

can be defined through the directly conversion of these cubic voxels. Each voxel is converted in a hexahedron-shaped 8-nodes finite element, usually called brick element, with the same dimension of the original voxel.

The bone tissue is considered to be isotropic, homogeneous and characterized by a linear-elastic behaviour, therefore the constitutive law for bone tissue is defined by only two parameters: elastic modulus E and Poisson ratio ν. For the elastic modulus a tentative value E_t^0 is hypothesized of 19 GPa, which corresponds to the E value assessed for compact cortical bone. It can be assumed as a reference for the tissue value that constitute the trabecular structure, and the Poisson ratio is set at 0.3 [50]. Coherently with the experimental tests, boundary conditions and external load are applied to the μFEM model.

FEM numerical solution

Boundary conditions are assumed to describe the constrains applied in the experimental test, the micro-FE model is solved with the ParFE (Copyright 2006 ETH Zurich) iterative solver. Parfe is an open source software characterized by a scalable and high parallelization finite element solver for bone modelling. Thanks to the geometrical regularity of the elements, Parfe implements a highly efficient solver on the element by element algorithm to evaluate the stiffness matrix [2, 3].

Then the following boundary conditions are defined: the bottom of the model are fully constrained leaving no degree of freedom, while at the upper surface vertical displacement is imposed to simulate an uniaxial compressive test.

However, the μFEM model does not reproduce the same boundary conditions of the experimental test. In fact in the FEM models, the constraint is idealized as a perfect one, but due to the presence of the endcups this conditions can not be verified. Moreover, the endcups influenced how the displacement is transferred from the actuator to the specimens and probably these behave as a dampers.

Post-processing

The Post-Processing gives information about the mechanical test simulation. According to the boundary conditions, it calculates the total reaction force R at the two constrained surface and considering the nodes at two height (z_1 and z_2), corresponding to the extensometer rubber bands, the mean displacements are calculated from the displacements of the selected nodes. Then the apparent elastic modulus (E_{app}^{FEM}) can be evaluated as the follow:

$$E_{app}^{FEM} = \frac{\frac{R}{A}}{\frac{\overline{u}_{z,2} - \overline{u}_{z,1}}{z_1 - z_2}} \tag{2.2}$$

Where A is the nominal cross-section of the specimen, L_0 is the initial distances between the extensometer rubber bands before the model solution and u_{z1} and u_{z2} are the displacements measured in correspondence of the extensometer knives at the levels z_1 and z_2. Since a linear model is adopted E_{app}^{EXP} is linearly related to the elastic modulus E_t^0, assumed for the tissue. Therefore the assessment of the actual value of E_t, which equals E_{app}^{FEM} with E_{app}^{EXP}, is given by the simple relationship:

$$E_t = \frac{E_{app}^{EXP}}{E_{app}^{FEM}} E_t^0 \tag{2.3}$$

Nowadays, these methods allow to obtain an estimation of E_t based on the combination of FEM models and experimental tests, which acquire information through punctual observation of the displacements field. In fact, these are measured in each test with an extensometer that registers the displacements relate to the contact areas between the instrument and the sample surface. Moreover, the instrument is linked to the sample with rubber bands which could alter locally the displacements field, and the extensometer knifes are inserted in the structure breaking trabecular elements that are not connected to the volume. These events are confirmed by several experimental tests and are related to the structure properties (BV/TV, BS/TV, $Tb.Th$), also they produce artefacts which reduce the correspondence between experimental reality and FEM models. In fact, the extensometer is not considered in the FEM model, where the sample is intact.

Actually, new technologies consent to evaluate the data acquired on a portion and not limited on a punctual measurements. The Digital Image Correlation allows to obtain information about the displacements fields without altering the sample surface, even though the effects of the paint used to allow the recognition of the sample geometrical patterns are under verification.

2.3 Overcome the limitations: the DIC.

3D Digital image Correlation is based on the optical acquisition of a sample during its deformation caused by mechanical or thermal loads. A system of sensors acquires photos (see figure 2.8) of the specimen during the experimental test at high frequency (typically 15 Hz). Thanks to the use of a stochastic

pattern on the sample surface, the DIC is able to identify a group of points on the object. Through correlation algorithms, this system is able to detect the position of each selected point for each frame, then an algorithm calculates the 3D displacement occurred between two acquisitions for each one of the detected points. In order to identify univocally a point, the object surface has to exhibit certain properties. The ideal surface patterns should not have an ideal orientation and should be non-periodic. Then these properties lead to the use of stochastic colour patterns on the sample surface which adheres and deforms with it. An important feature of speckle patterns is their high information content, allowing the use of small aperture for pattern matching, commonly called subset or facet [47, 7, 10, 22, 29].

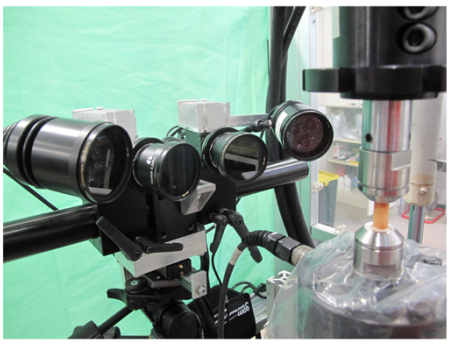

Figure 2.8: DIC system composed of two digital CCD cameras and LED lights.

Facet

Every image is divided in several pixel subsets, referred to facets. Usually, facets have square geometry NxN, where N is the side dimension called *facet size*. Due to the facet step an overlay can occur and the result is an overlapping area. The dimension of the overlapping area impacts on the probability that the facet is correlated in the different frames 2.9. Moreover the facet size affects the computational time for the measurement. In fact, larger facets lead to higher computational time but the measurements are more accurate and the noise related to digital acquisition is low. Instead, smaller facets allow to appreciate local effects, but there is a high probability to have uncorrelated area and noise is amplified.

Stereo vision

To obtain the 3D displacement fields a stereo-vision system is used. Stereo vision is based on the use of two cameras which register a scene in a synchron

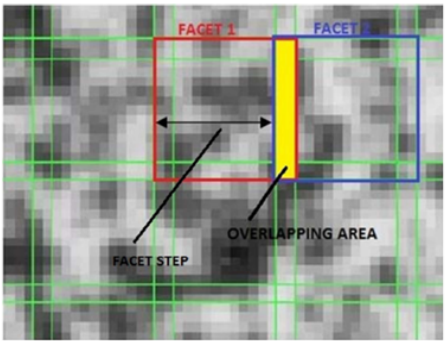

Figure 2.9: Facet size (15 x 15 pixels), facet step (13 x 13 pixels) and overlapping area

manner. Considering the figure 2.10, stereo vision allows to find homologous point r' and p. In fact thanks to the epipolar geometry, knowing the camera positions, only one plane passes through the optical centers C and C' and the point of interest R [27][40]. A fundamental step for the triangulation

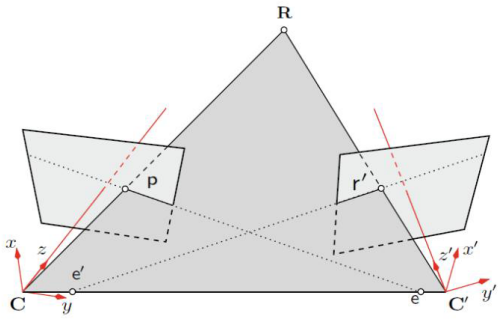

Figure 2.10: Stereo vision

success is the matching stereo, in fact it consents to identify homologous points in two stereo vision images. The research of the homologous points leads to construct the disparity images, which allow to find easily the depth of each point in the image. Different algorithms can be found in literature to solve the stereo matching, and they can be roughly divided in two categories: feature-based and dense stereo. The first ones recognize some image features, such as points lines or edges, then these algorithms allow to reconstruct only the features of an image. Moreover the dense stereo algorithms realize a disparity map for each point of the image. The disadvantage of this family of algorithms is that the reconstructed map is not dense. In other words the disparity is not found for all points and this leads to uncorrelated problem.

Calibration

The calibration process allows to measure the camera parameters: intrinsic and extrinsic parameters. Intrinsic parameters refer to the shape and dimension of the CCD sensors and their respective orientation. Instead extrinsic parameters give information about the 3D orientation of the cameras and allow to obtain the prospective transformation from the 3D space to their reference system. The calibration is easily done using calibration panels (see figure 2.11) under different perspective views. These panels have particular pattern with fixed geometrical features, then the system registers point positions and evaluates extrinsic and intrinsic parameters with specific algorithms [40].

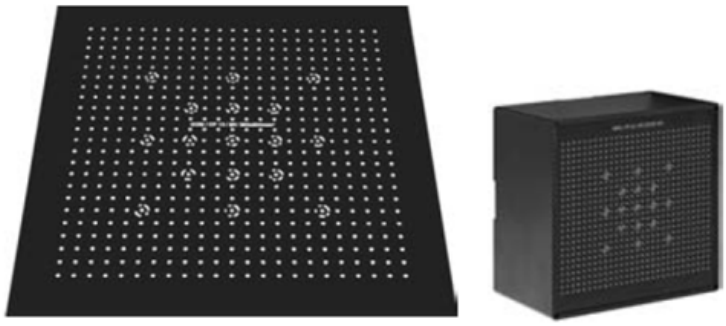

Figure 2.11: Calibration panel used to measure camera parameters.

Noise in digital image

DIC is affected by digital noise due to the CCD sensors of cameras, and it can be classified in thermal noise, 1/f , bias noise and quantization noise.

- Thermal noise: is the noise generated by the charge carriers inside an electrical conductor. This type is sometimes called “white” noise, because its magnitude is indipendent on frequency.

- 1/f or flicker noise: it has an approximately inverse dependence on frequency.

- Bias noise: the CCD has a varying sensitivity from pixel to pixel, then it measures the difference between the pixels.

- Quantization noise: it is caused by the digitalisation of the signals coming from CCD.

DIC measurements are affected to the noise, which causes errors in the evaluation of displacement fields, then in order to obtain an accurate measurement it is necessary to minimize or evaluate it.

Aramis-Materials

The DIC acquisition device in use at Laboratory for Medical Technology is GOM mbH ARAMIS 5M (fig. 2.12), and it is principally composed of the following parts:

- 2 digital black-white CCD cameras
- system of LED lights
- sensor's controller and acquisition board
- tools for DIC calibration

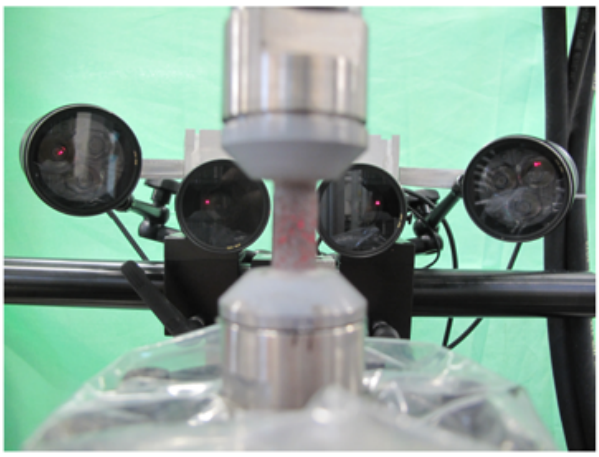

Figure 2.12: Aramis system.

This system is used to acquire the images from the mechanical tests of trabecular bone. As we have already seen, a high contrast pattern is required for an accurate point detection [17]. The stochastic pattern is applied in two steps: first, a homogeneous white paint is applied to the trabecular surface. Secondly, black acrilic paint is applied randomly (see figure 2.13). Subsequently mechanical tests are performed as explained in the previous paragraph (2.2.2) and during the test, Aramis acquires images in order to measure the surface displacements of cancellous bone. The principal steps of the compressive tests are the following:

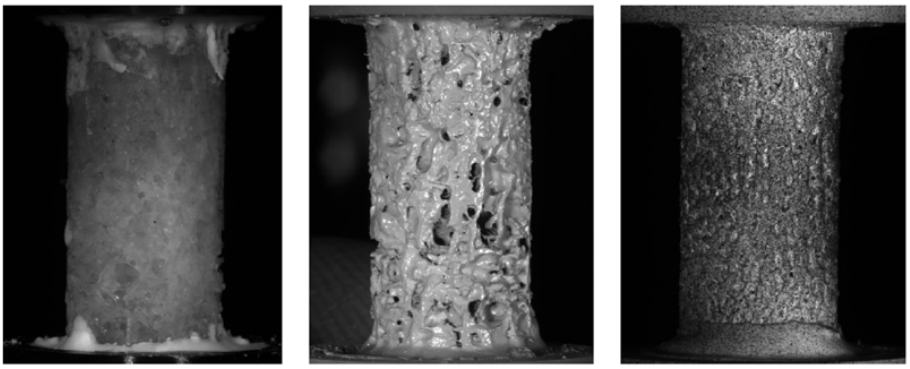

Figure 2.13: The first image on the left shows the specimen's acquisition before the application of the pattern, the central image shows the specimen after the application of white water paint and the last image after the application of black stochastic pattern.

1. A precondition load/unload cycle is performed in order to avoid plays between specimen and PMMA and between cement and machine joints;
2. The compressive test is performed four times for every angular position according to the landmarks. In this step the displacements are measured with the extensometer.
3. For each angular position, images are acquired with Aramis system.

All the compressive tests are performed with a strain rate of 0.1s which is controlled by the testing machine(INSTRON 8502, Instron Corp.,Canton,MA). According to [27] the optimal parameters to acquire biomedical images are the following:

Table 2.1: DIC parameters

Facet size [pixels]	35
Facet step [pixels]	10
Field of view $[mm]$	25x21
Shutter time $[s]$	0.1

Critical points

There are several problems related to the DIC acquisitions.

1. Due to the anisotropic structure of the trabecular bone and dimension of the specimens (see figure 2.14), DIC algorithm can not find the

homologous points in the images of two cameras. Although the accurate calibration of the system, the features of this application are highly different from the range of measure imposed by the Aramis developer. In fact this system was developed to measure displacements in the range of mm, but this analysis leads to displacements in the order of μm. Due to the specimens shape, the field of view of the two cameras is limited, and only a little part of the samples is acquired from the system.

2. The patterns on the specimen surface create a layer which caused a thickening of the sample. Because of this problem, the nominal dimension of the samples are changed and it could vary the mechanical proprieties of bone. Moreover, DIC measures points displacements, but due to the patterns it could not measure bone displacements, but paint's point displacements.

3. The paint filled the hole on the surface and this lead to have points in some region in which in the bone structure there is a hole. For this reason the surface results altered, and in order to register FEM and DIC models, it causes a problem to recognize correspondent regions.

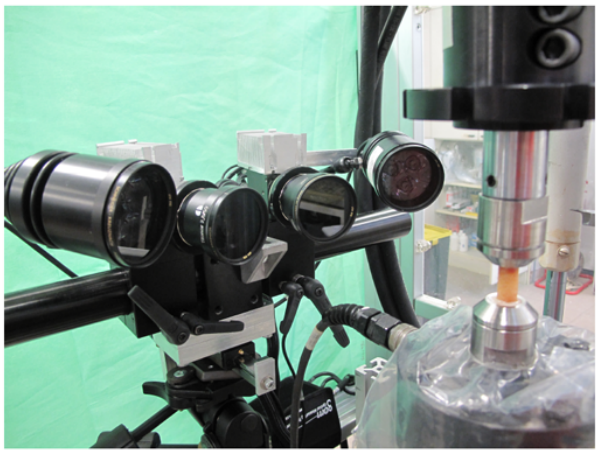

Figure 2.14: DIC field of view.

2.4 Aim of the study

DIC and μFEM methods show trabecular bone displacements calculated in two independent manner. The aim of this work is to define a method to correlate the measurements obtained with the two techniques (the figure 2.15

summarizes the procedures to obtain respectively FEM and DIC displacements field).

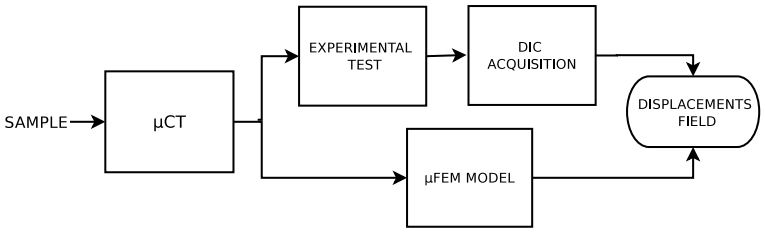

Figure 2.15: Flow diagram.

This is an explorative study which would lead to several results.

1. Due to the simplified boundary conditions applied to the FEM model, and to the unknown behaviour of the end cups, which probably don't act in a linear manner, it is not possible to proceed with the validation of the FEM model. However, the comparison of these two independent method could lead to the FEM verification, that is the investigation of the coherence of FEM models with the experiment.

2. The DIC measurements could be used to obtain an accurate estimation of the tissue proprieties of the trabecular bone and in particular the tissue elastic modulus E_t. In fact, the information acquired with this methods are related to the sample surface rather than punctual measurements of the extensometer.

Chapter 3

Comparing FEM and DIC displacements

In the previous chapters the methods to obtain FEM model and DIC acquisition and details of the experimental tests are described. The results of FEM models are affected by several critical uncertainty, due to the approximation in defining the boundary conditions and to uncertain measures extract from the experimental tests which register punctual displacements with the extensometer. In order to overcome these obstacles another technique is used: the Digital Image Correlation (DIC). In fact this method allows to obtain a different measure from the extensometer based, monitoring displacements over a whole surface of the sample rather than over a single couple of points. However, there is not an algorithm available which allows to register DIC data over FE model. In this chapter a method to compare displacements field of numerical model and DIC acquisition is described.

3.1 Registration algorithms

Image registration is a geometrical transformation which allows to align points in one view and the corresponding points in another view of the same scene. Given two images, usually referred as *template* and *reference*, the registration technique has to find a spatial transformation such that the template matches the reference image.

Registration can be applied to multidimensional images, acquired by different sensor type, or mono-dimensional acquired by the same sensor type. Generally, registration is necessary for: images of the same scene acquired from different points of view (*multiview analysis*), images acquired at different times (*multitemporal analysis*), images referred to different acquisition

modality (*multimodal analysis*).

Registration methods can be classified considering the technique used to compare the input images [52][16].

Manual registration: It requires specific software to easily handle the images. This approach has many disadvantages, the most important is that is user-dependent, so the degree of accuracy could vary user-to-user.

Landmark-based: It allows to identify the landmark position in the corresponding images and calculate the transformation which aligns these points.

Surface-based: It requires the recognition of surfaces from the images; a transformation for the minimization of the distance between the two surfaces is calculated.

Intensity-based: It is the most widely used technique allowing to evaluate the image pattern with correlation metrics. There are two principal approaches: the first is to reduce the image to a set of scalar, the second is to use the full image content throughout the registration process [24].

3.1.1 Algorithms

In the last decades, many algorithms were developed to resolve registration tasks, nevertheless lots of them are application-dependent. The mainly used algorithm, considered a golden standard, is the Iterative Closest Point Algorithm (ICP). It was proposed by *Besl et al.* [5] in 1992 and was developed to minimize the difference between two surfaces. Several statistical metrics are applied to improve the robustness of this algorithm, leading to the development of different solutions, and one of these is the Trimmed Iterative Closest point algorithm (TrICP). Actually the TrICP is preferred because it is less sensitive to local effects, but in our particular problem TrICP and ICP algorithms can not resolve the registration task (further information on these algorithm are reported in the appendix C). There are several problems related to the application of these algorithms. The noteworthy reason is that they require a preregistration of the two points clouds. The spatial configuration of FEM and DIC points sets is not predictable, and if a preregistration was required, it means that specific algorithm would be developed [28, 19]. Furthermore, the points sets have notable resolution differences and there is not a correspondence among the points sets, which makes difficult to obtain stable and robust results with these algorithms.

3.2 FEM and DIC points sets registration

As described in the chapter 2, FEM and DIC points sets are obtained from two different procedures, then several discrepancy can be catalogued.

FEM models represent the entire specimen's volume. Even if an external shell of fixed thickness can be isolated, this will still contain both superficial and internal points. Furthermore, due to porosity of the trabecular bone specimens, there is not an algorithm to easily detect the boundaries.

On the other hand DIC data sets are composed only by the external point of the specimens. In fact, it is derived from an optical reconstruction, and exclusively the most superficial points are acquired. The great dissimilarity in thickness and number of points conducts to complicate the points alignment.

Moreover, due to the stochastic patterns on the sample surface of DIC models, that constitutes a physical surface on the sample, some artefacts can be introduced. These lead to the reconstruction of DIC's points in the regions correspondent to the holes of the bone surface. In other words, they have not a correspondence on the FEM points set and in order to register the models, it is impossible to recognize similar structures.

Another significant obstacle is the DIC acquisition. As reported in chapter 2, trabecular structures are smaller than the dimensions typically suggested by the Aramis constructor for obtaining accurate measurements. In fact, the system obtained uncompleted maps of the specimens, because of the difficulties to recognize for every single point the homologous one. Then this problem could lead to a lack of correspondence between points from the model and those from the DIC acquisition.

Due to all these problems it was necessary to develop a specific algorithm to resolve the registration task.
First at all, geometrical correspondences are found. Angular position of the bone specimens are identified with five landmarks, as shown in the figure 3.1, and this reference system is acquired with the μ-CT scanner. The DIC system acquires only a portion of bone specimens included in the field of view, and the set up is arranged to include in front of the DIC camera an aluminium sphere in each acquisition. The sphere is individuated on the FEM model and the correspondent angular portion, which includes the landmark, is extracted from the FEM model. Another important feature is that DIC data set is acquired from a cylindrical specimen, and thanks to the stereovision, which allows to reconstruct the 3D spatial arrangement of the data obtained, the points are distributed in a cylindrical shape. Since it would be easier to do a registration if the point sets fitted the same 3D shape, a cylindrical fitting can be performed on the DIC points cloud.

The registration task can be divided into the following steps:

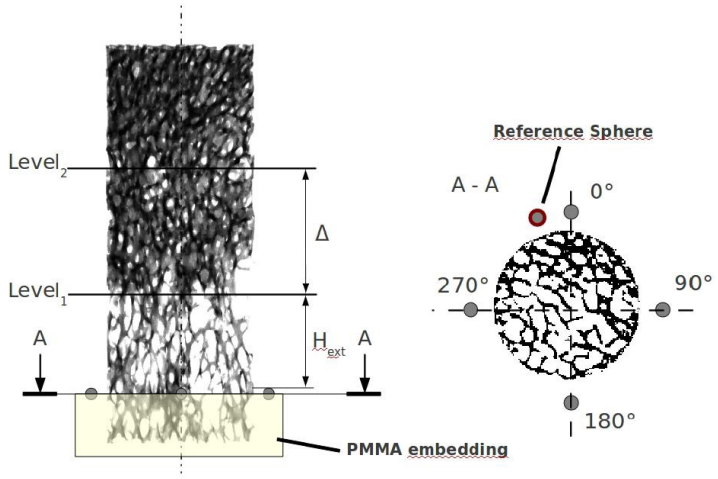

Figure 3.1: Aluminium landmarks allow the repetition of the test along four different angular position at 0°, 90°, 180°, and 270°.

- Cylindrical fitting of point cloud from DIC acquisition.
- Define an angular sector of the FEM model.
- Calculate the equation of symmetry axis of FEM model with 3D linear regression.
- Evaluate the registration parameters and then apply the rigid transformation.

3.3 Working on DIC points cloud

Thanks to the stereovision DIC points cloud is arranged in a 3D cylindrical shape. Due to several problems, such as the particular micro-structure and the limiting boundary conditions of the DIC acquisition, displacements field is affected by noise. In the following paragraphs the points set is fitted on a cylindrical surface and the displacements field is analysed and some vectors are excluded to reduce the noise.

3.3.1 Cylindrical fitting

Bone specimens have cylindrical shape and DIC data sets are organized in a 3D grid of points which reproduces their cylindrical form. So these points

cloud can be attributed to cylindrical geometry evaluating its principal characteristics: radius, the direction of symmetry axis and a point on it. In order to obtain the best fitting of the DIC points on a cylindrical surface, an error function is implemented and minimized.

An infinite cylinder is defined by an axis determined by the unit-length vector **D**, containing the point **C**, and a radius **r** >0. A right-handed orthonormal set is defined (U, V, W), where all the vectors are unit-length and mutually perpendicular. Supposing X_i with i=1:n be the input point set, a least square error function for cylindrical fit can be estimated as:

$$E(r^2, C, W) = \sum_{(1:n)} [(X_i - C)^T (I - DD^T)(X_i - C) - r^2]^2 \qquad (3.1)$$

it involves seven parameters, one for the radius **r**, three for the point coordinates **C**, and three for the unit length vector **D** which rapresents the axis direction [14]. In order to evaluate the optimal cylinder which fits the points clouds, these parameters are obtained from the minimization of the least squares algorithm. Further details are reported in appendix A.

3.3.2 Image filtering

Due to the numerous limiting factors associated to DIC measures, the images obtained show noisy fields as shown in figure 3.2. In fact, DIC obtains good measurements in the plane in front of the cameras, while in orthogonal plane the measured displacements are imprecise and inaccurate. Thus, it is necessary to filter the displacement fields, in order to eliminate the vectors out of the ordinary.

Considering the arrangements of the displacements field, all the vectors are expected to be aligned with a common direction. Particularly, they are arranged in parallel to the symmetry axis of the cylinder. The outliers, shown in the figure 3.3, are organized on different direction compared to the other vectors and also their components have a very different magnitude. A way to identify and eliminate these vectors is to consider the angles included between the axis and the vectors. The angles are distributed on a restricted range as shown in the histogram 3.4, while only few vectors have angles out of the ordinary, that are represented in the right tail. Thus, all the vectors associated with angles included in the right tail are eliminated, considering the percentiles of the distribution. In this manner all the outliers are excluded, without a significant reduction of the initial information and keeping intact the other vectors of the displacements field.

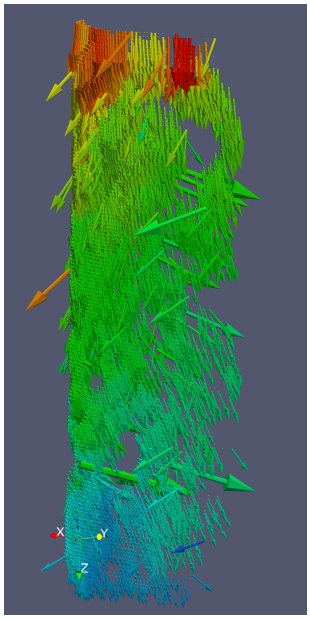

Figure 3.2: The major part of the vectors have the same direction, while several vectors have differ deeply from the first ones.

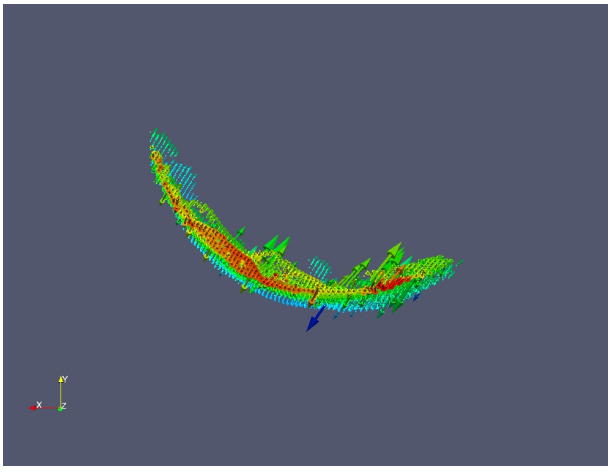

Figure 3.3: Figure shows a particular view of the points cloud and the displacement fields with out of the ordinary vectors.

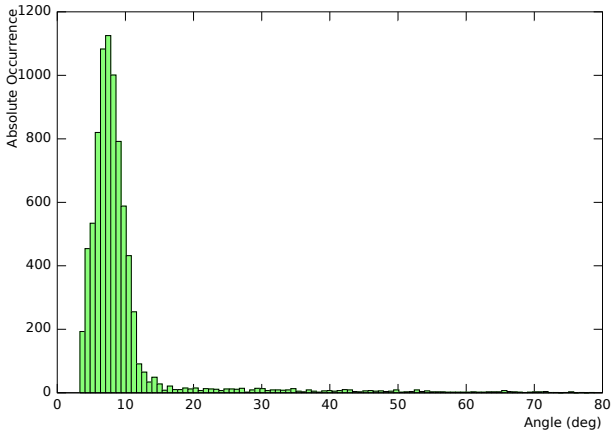

Figure 3.4: Histogram shows the angle distribution for DIC displacements field.

3.4 Working on FEM models

The 3D reconstruction of trabecular bone structure represents the whole bone volume. Two principal operations have to be carried out on FEM models. The first one is to calculate the symmetry axis of the cylindrical sample which can be used to overlay DIC and FEM data sets. The second is to extract an angular section of the specimens in order to reduce the number of points and the computational costs of the procedure.

3.4.1 3D Linear regression

Trabecular bone is a porous material, and its mass is not evenly distributed in the volume. The section is notched and the specimens could be acquired in the μCT with a misalignment in respect to the scan axis, and the section of the specimen could be an ellipse. So it would not be easy to detect an envelope circumference around the specimen. For these reasons the axis of symmetry of a cylindrical shaped specimen can not be merely calculated as the axis of symmetry of the entire volume, but we have to take into account the micro structural variation due to nature of material and those introduced with the modelling procedure.

Dividing the FEM models in thin slices (thickness 0.5 mm), the centre of gravity is calculated for each section and then the best fitting straight line, which passes through these points, is calculated. A linear least squares fitting technique does not provide a solution to this task. Although linear least square furnishes good solutions to 2D linear regression, in this case it is required an analytical solution to 3-D linear least square fitting.

Considering the points coordinates P_k, the orthogonal projection of P_k

on a straight line L is H_k and the perpendicular offset is $d_k = P_k H_k$. The fitting problem is to find $\mathbf{L}$ so that minimize $\sum d_k^2$,and the analytical solution of this problem is explained in the appendix B.

3.4.2 Angular section

In order to compare the models obtained with FEM and DIC techniques, a thin angular section of the specimens has to be extracted (see figure 3.5). The angular section is selected considering the angle subtended by the DIC points cloud and then it is pulled out from the entire volume. In this manner the computational costs are reduced and only the region correspondent to the DIC model is considered.

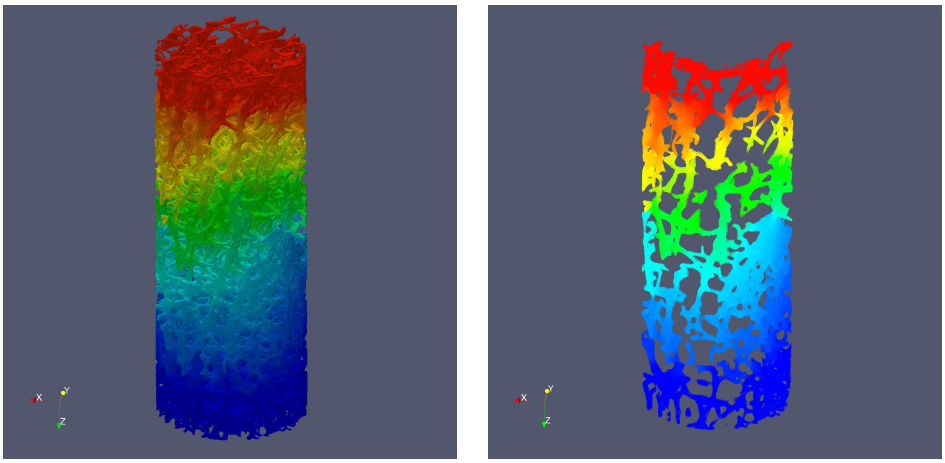

(a) FEM volume (b) FEM angular section

Figure 3.5: The image on the left shows the entire FEM model, while the image on the right represents an angular section of the bone model.

3.5 Rigid transformation

DIC points cloud and FE model are produced from separate procedures and for this reason they are referred to different reference systems. In order to overlay DIC points on FEM cloud, a specific algorithm was developed and the main features are given in this paragraph.

A geometrical transformation $\mathbf{T}$ is a function mapping a set of points coordinates to another one or to itself:

$$x' = \mathbf{T}(x) \tag{3.2}$$

The set of possible transformation $\mathbf{T}$ may be divided into rigid and non rigid transformation, and the latter can be divided in many subset (affine, scaling, perspective, curved). Rigid transformations are defined as a geometrical transformation which allows to preserve distances and preserve the straightness of lines. This class of transformation allows only rotation and translation of a coordinate system and it requires only two parameters: the translation vector $\mathbf{t}$, and the rotational matrix $\mathbf{R}$. Then the trasformation can be expressed by the following equation:

$$x' = \mathbf{R}x + \mathbf{t} \tag{3.3}$$

In 3D space, three angles of rotation $(\theta_x, \theta_y, \theta_z)$ can be individuated, called Euler angles, and consequently the rotation 3×3 matrices can be defined as follow:

$$R_x = \begin{bmatrix} \cos\theta_x & -\sin\theta_x & 0 \\ \sin\theta_x & \cos\theta_x & 0 \\ 0 & 0 & 1 \end{bmatrix} \tag{3.4}$$

$$R_y = \begin{bmatrix} \cos\theta_y & 0 & \sin\theta_y \\ 0 & 1 & 0 \\ -\sin\theta_y & 0 & \cos\theta_y \end{bmatrix} \tag{3.5}$$

$$R_z = \begin{bmatrix} 1 & 0 & 0 \\ 0 & \cos\theta_z & -\sin\theta_z \\ 0 & \sin\theta_z & \cos\theta_z \end{bmatrix} \tag{3.6}$$

In this case, considering the two cylinders fitted, six degree of freedom (DoF) are associated to their configuration (three for rotation, three for translation). To obtain their registration, it is necessary to reduce to zero these DoF, reaching the perfect overlay. As discussed in the previous paragraph 3.3.1, after fitting of a cylindrical surface on the cloud of points from DIC acquisition, it is possible to obtain the direction of symmetry axis and the cylinder radius. Additional geometrical information can be obtained from the coordinates of the centres of the spheres.

The algorithm developed allows to evaluate the 3D arrangement and reduce the DoF thanks to the information furnished by the previous procedures. The reference sphere is considered first. The distance vector between their centers (into FEM model's reference system and DIC acquisition, respectively) is calculated. This will correspond to the translation vector. In this manner, the number of DoF is reduced to three degrees, related to the rotation angles.

The second important information is the vector associated to the symmetry axis. Keeping fixed the two spheres, the axis related to FEM and DIC

fitting can be aligned evaluating the angles comprised between the geometrical features mentioned above. Once the three angles and the translation vectors components are evaluated, the equation 3.3 can be calculated and the overlaying is achieved.

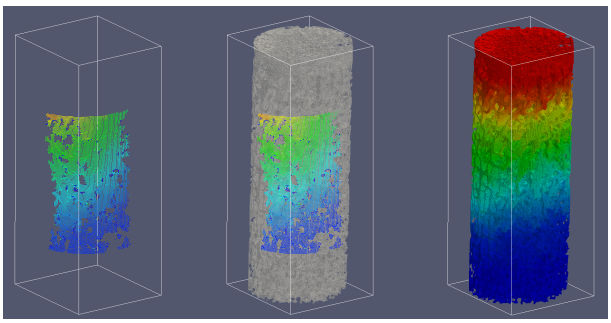

Figure 3.6: Image represents on the left the DIC points cloud, on the right an entire FE model and in the centre the registration between the data sets.

3.6 DIC and FEM displacement fields comparison

Once the DIC data set has been registered to the FEM model, the displacement fields can be compared. The distance between DIC points is about 100 μm, while it is about 39 μm for FEM according to the resolution of the model. Then a strategy was studied to compare the fields considering the different number of points in the two points sets. The methods adopted are described here:

- projecting each DIC point on the FEM points cloud a correspondent volume is individuated.

- the point represents the center of symmetry of the volume and thanks to geometrical considerations all the nodes included in a distance of 50 μm are take into account.

- the mean values of the displacements field are calculated for each volume portion and they are associated with the values of displacements of the DIC point.

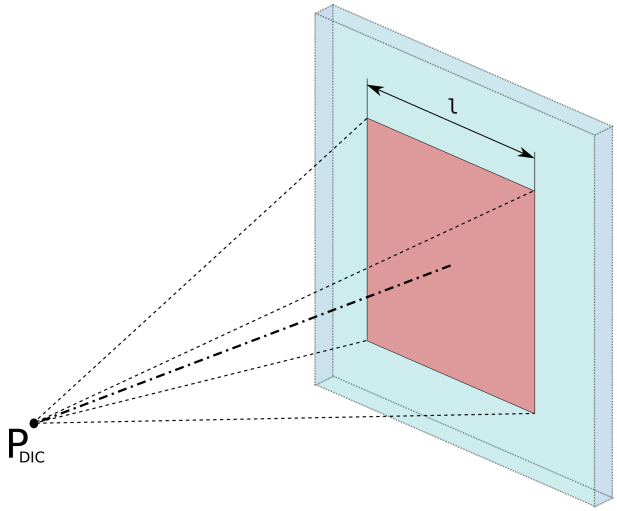

Figure 3.7: Image represents the projection of DIC point on FE model and the volume considered.

3.7 Findings

Once the correspondent values for the data points sets are obtained, it is possible to compare and evaluate their relationships. In the following paragraphs the goals of this work and the methods used to analyse the results are described.

3.7.1 Goals

According to the aim of this thesis, the following main issues have to be examined.
The coherence between DIC and FEM displacements. As mentioned in the chapter 2, due to the simplified boundary conditions applied to FE models and the unknown behaviour of the end cups, the numerical models do not completely reproduce the boundary conditions. All the data derived from the experimental tests are used to solve the FE models, so there are not independent information to verify the trabecular bone models. For these reasons FE models of trabecular bone specimens are not validated.
In addiction, due to the end cups the real displacement imposed on a sample can not be evaluated. The developed numerical models are based on the linear assumption between strain and displacements, so these models are solved imposing an arbitrary displacement.
On the other hand, DIC frames are acquired with the same set up of the experimental tests and they give information about the displacements fields

over a whole aspect of a sample. In order to evaluate the accuracy of the FE models, the displacement fields associated to numerical models and DIC acquisitions can be compared. So comparing DIC and FEM displacement fields would be a way to evaluate the coherence between experimental tests and FE models.

The value of the tissue elastic modulus E_t of the trabecular bone. This modulus is calculated with the data obtained from the extensometer which is affected by several problems. The extensometer registers the displacements related to the contact areas between the instrument and the specimen surface, but it is a punctual measure on a heterogeneous material thus the measure could be affected by local artefacts and influenced by local alteration of the displacements. Comparing DIC and FEM displacements could lead to another estimation of the tissue elastic modulus and this method has several advantages. The tissue elastic modulus obtained with this technique would be independent of the extensometer measurements and DIC displacements field furnishes information about an entire aspect of the specimen rather than the extensometer.

3.7.2 Results analysis

Due to the different displacements applied in the FE models and experimental tests the values obtained are referred to different scale. The first step to compare these techniques is to calibrate FEM and DIC displacements.
A linear regression is applied to these two point sets and the regression parameters are evaluated to scale FEM displacements in the same range of DIC displacements. Thus the FEM displacements field is multiplied by a constant β, calculated as the regression coefficient of the variables, in this manner the data sets are expressed in the same range of values.
In order to evaluate the coherence between DIC and FEM displacement fields the coefficient of determination R^2 was calculated. R^2 indicates if the fit of the model is or is not satisfactory 3.8. Moreover the goodness of fit was evaluated analysing the residuals. The percentage of residuals at several values of the cumulative error function were considered as shown in the figure 3.9.

Once the coherence is evaluated, the second goal is to estimate the tissue elastic modulus. A parameter γ is calculated as:

$$\gamma = \frac{R_{EXP}}{\beta R_{FEM}} \tag{3.7}$$

where R_{EXP} is the reaction force applied to the sample during the frame acquired through the system; R_{FEM} is the total reaction force calculated in FEM model at the constrained nodes correspondents to the end cups; β is

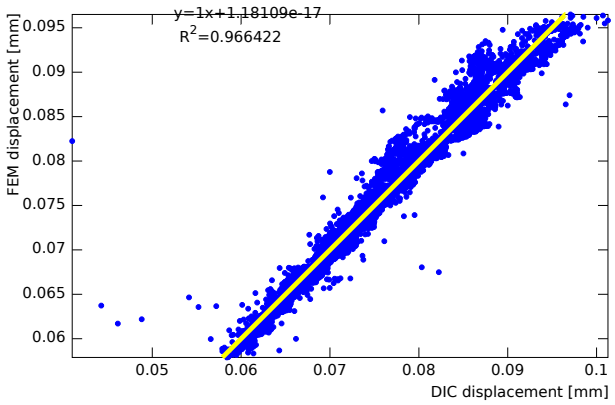

Figure 3.8: Graph shows the trend of FEM and DIC displacements.

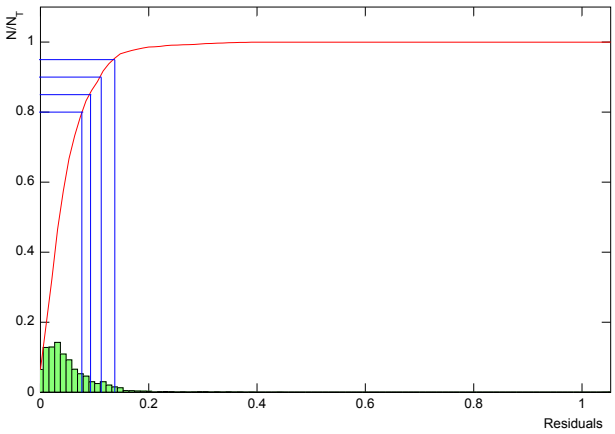

Figure 3.9: Figure shows the histogram of the residuals and the cumulative error function. The correspondent values to 80% 85% 90% and 95% of the error function are individuated on the histogram.

the constant evaluated as regression parameter. Thanks to this constant a new value of E_t^{DIC} is furnished, evaluated as:

$$E_t^{DIC} = \gamma E_t^0 \tag{3.8}$$

where E_t^0 is the value adopted for the tissue proprieties to solve the FEM model. Due to the definition of the FE model, which is defined up to a constant, this comparison allows to find E_t^{DIC} that is the value of tissue elastic modulus to fix in the model.
Once obtained E_t^{DIC}, the second goal is pursued. The estimations of E_t^{DIC} are compared with the estimation of the tissue elastic modulus obtained with the extensometer. Two estimations are considered: the first one obtained as the mean value of tissue elastic modulus over all the repetitions ($\mathrm{E}_t^{ext,m}$), the second estimation obtained on the single aspect correspondent to DIC aspect (E_t^{DIC}).

Chapter 4

Results

In the chapter 3 the method to reach the overlay of FE models and DIC acquisition is described. In the first part of this chapter a brief introduction is given about the procedure used. The results obtained to evaluate the coherence between DIC and FEM displacement fields are reported, and in the latter section sensitivity studies are discussed in order to evaluate the robustness of the parameter chosen.

4.1 Material and methods

20 specimens (10.0 mm diameter and 26 mm in length) were extracted from human femoral condyles of four different donors. A PMMA endcup was realized onto each end of all specimens and aluminium spheres were positioned in the cement in order to use them as landmarks. Finally, the samples were immersed in Ringer solution for micro-CT scanning. Trabecular specimens were acquired (Skyscan 1072®, BRUKER, Kontich, Belgium) using a standard protocol [35]: 50 kVp, 200 μA, 1 mm aluminium filter, exposure time 5.9 s, rotation 180°, rotation step 0.9°, field of view 20 mm x 20 mm and isotropic pixel size 19.5 μm. The specimens length exceed the field of view, so two different scans of the same specimens had to be acquired and successively glued to reconstruct the entire volume. Cross section images were reconstructed in 8 bit format, 1024 x 1024 pixel in size.

4.1.1 Experimental tests

The experimental compressive test layout was performed in order to avoid end artefacts and systematic errors, following the layout developed at the Rizzoli's Orthopeadic Institute facilities [17, 33]. The compressive tests were

performed under displacements control at a deformation rate of 0.01 s^{-1}, while an extensometer was attached to the central part of the specimens and its angular position and height are registered in respect to the aluminium spheres (see figure 4.1). Finally the apparent strain and E_{app}^{EXP} are evaluated.

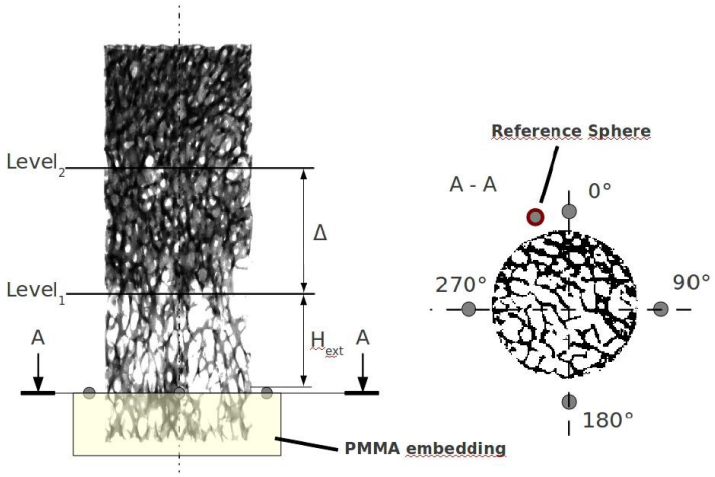

Figure 4.1: Experimental layout scheme: the reference spheres allow to find the extensometer knives levels and the angular position.

4.1.2 DIC acquisition

As described in chapter 2, the digital image correlation is based on the optical acquisition of a sample during a mechanical test. In order to allow the recognition of group of points on the object, a homogeneous white covering in water paint was applied to the surface then a stochastic pattern was realized with black acrylic paint [27, 17]. Finally the system was set and accurately calibrated. The characteristics of the DIC data acquisition are reported in table 4.1.

Facet size [pixels]	35
Facet step [pixels]	10
Field of view [mm]	25x21
Shutter time [s]	0.1

Table 4.1: Features of DIC data acquisition during mechanical compressive test.

Subsequently, bone specimens were tested to uniaxial compression during monitoring of the system. 4 cycles were realized with the specimen in the

same position and the system acquired 50 frames, one per second, following the evolution of the displacement fields on the surface. Then for each frame the displacements field was calculated referring to the first frame which is referred as undeformed state.

4.1.3 Micro-FE models

On the basis of previous studies [35], a grey scale value of 117 was used to apply a global threshold on the μ-CT stack. Then to reduce the computational costs, the data set can be re-sampled to lower resolution, from 19μm to 39μm, and finally a connectivity test was applied. Each voxel of the micro-CT images were converted in a hexahedral elements with a resolution of 39 μm. Boundary conditions were imposed to the model according with the mechanical test layout. All nodes laying at the bottom cement surface were fully constrained, while the nodes on the upper cement surface of the model had vertical displacements imposed and horizontal displacements forbidden in order to simulate the uni-axial compressive behaviour of the experimental test. FE models were solved with ParFE multilevel iterative solver (Iteration limit = 1e6; Tolerance = 1e(-9)). The apparent elastic modulus was calculated as:

$$E_{app}^{FEM} = \frac{\frac{R}{A}}{\frac{\overline{u}_{z,2} - \overline{u}_{z,1}}{z_1 - z_2}} \tag{4.1}$$

Where R is the reaction force at the constrained surfaces and A is the nominal cross section of the bone specimens, $\overline{u}_{z1}$ and $\overline{u}_{z2}$ are the average value of axial displacements measured at the levels z_1 and z_2 of the extensometer knives (see figure 4.1).

4.1.4 Cancellous tissue modulus

E_{app}^{FEM} is linearly dependent on the value E_t^0, and the elastic modulus of the cancellous bone tissue was calculated imposing that E_{app}^{FEM} equals E_{app}^{EXP}, then it is evaluated as:

$$E_t = \frac{E_{app}^{EXP}}{E_{app}^{FEM}} E_t^0 \tag{4.2}$$

Where E_t^0 was set at 19 GPa.

4.1.5 Registration of DIC measures on FEM model

In this section the procedure to register DIC points cloud on the FE model are summarized and the parameters used to post-process FEM and DIC data sets are presented.

- In order to compare the points clouds, the same surface of the DIC points cloud was located on the FE model, identifying the correspondent spheres. Then the symmetry axis of the FE model must be calculated and an angular portion of the cylindrical specimen was selected. It is not available an algorithm that allows to detect only the external surface of the FEM model and due to the porous structure a layer with a thickness of 0.9 mm was extracted to maintain information related to the surface.

- DIC points cloud is fitted on a cylindrical surface minimizing a least square error function as described in the appendix A obtaining data about the cylindrical axis, a point on the axis and the radius. Once the cloud was related to a standard geometrical shape, the points sets could be registered following rigid transformation.

In the chapter 3 further details are given about the methods used.

4.1.6 FEM and DIC displacement fields comparison

In order to compare DIC and FEM point clouds, in the DIC field must be excluded noisy components. The procedure is based on the evaluation of the vectors direction and the displacement vectors with components directions significantly different from the average direction were excluded. The distribution of the angle included between symmetry axis and vectors, which identify the direction of the vectors, was evaluated and the vectors that exceeded 90th percentile are excluded. This value was chosen in order to exclude the vectors that alter the displacements fields but at the same time maintaining a large amount of points.

Each DIC point was projected on the FEM model and a correspondent volume was individuated. These volume is characterized by a square surface, where the side dimensions are chosen according to the distance between the DIC points. The projected point constituting the barycentre of this surface and in order to cover all the region between one points and another, considering that the DIC resolution is 100μm, a side dimension of 100μm was selected.

4.2 Results

According to the aims of this study, the coherence between DIC and FEM displacement fields and the value of tissue elastic modulus obtained comparing these methods are evaluated. 20 specimens were extracted from four different donors (5 for each donor), but due to the following reasons 8 specimens are excluded:

- three specimens were crashed during the experimental tests (identification number: 4297_04, 3121_02 and 3016_05);
- in three cases it was evaluated that DIC system did not acquire accurately the displacements (3016_01 and 3016_02);
- in other two cases the extensometer measure was not significant (3016_04 and 4297_03).

Therefore, only 12 specimens were evaluated.

4.2.1 Coherence

The coherence between DIC and FEM displacement fields were evaluated. The results obtained were examined applying a regression analysis between displacement fields and residual analysis was performed. The results are reported in table 4.2, and they show that a high correlation among the displacement fields were registered. Only in two samples the coefficients of determination differ significantly (4297_02 and 3121_01) from the other values. In the sample 3121_01, the low correlation might cause for the high heterogeneity of the structure, which is evident both in the 4.4 and as shown in figure 4.2 in the aspect acquired with the DIC there is a lack of consistence of the trabecular structure over the surface. This problem would lead to acquire displacements which are not directly related to the structure, in fact the pattern covers all the holes and probably the paint's displacements are registered. In the other case (4297_02), structure singolarity are not observed and this problem would be related to the technological limits of the DIC and to its setting. In fact the DIC system was developed to acquire frames from a plane specimen, with a homogeneous structure and displacements registered in the order of mm. Conversely, the trabecular bone specimens have cylindrical shape, a porous structure and the curving surface is compared to the field of view of the cameras. Finally the displacements are registered in order of μm. Moreover, the applied pattern is characterized by several problem because of the set up is not optimized for this particular application

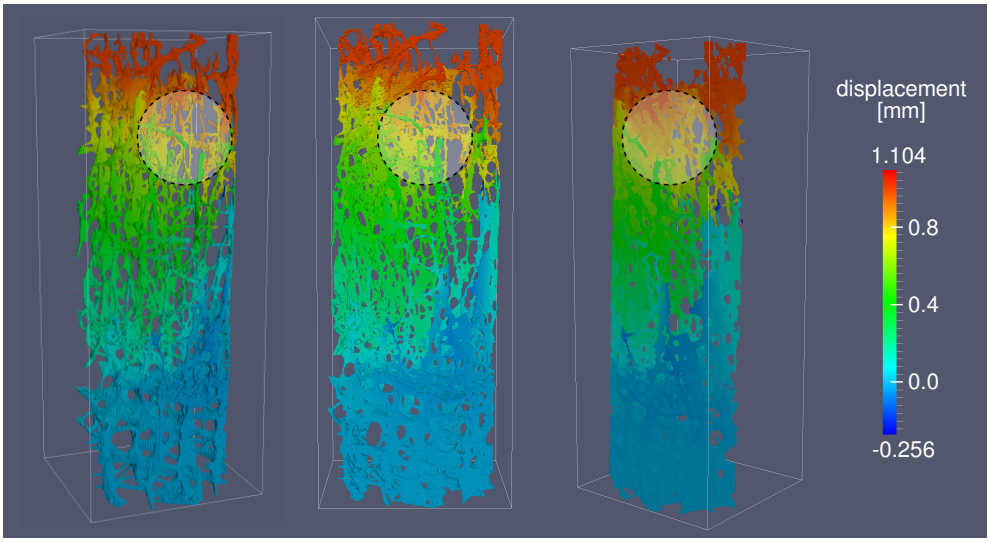

Figure 4.2: The image shows the sample 3121_01. Three different views of the aspect acquired with the DIC are represented. The lack of consistence of trabecular structure over the surface is evident in all the images.

and the dimension of the dots is not controlled. In fact, the parameters of this system are chosen in respect to the nominal dimension of the dots, then the measure could be altered.

Sample	$\mathbf{R^2}$	**Initial points**	**Filtered points**	**Points compared with FEM**
3029_01	0.93	7719	6947	5463
3029_02	0.84	8587	7729	4364
3029_03	0.95	9289	8360	4791
3029_04	0.97	7162	6446	4031
3029_05	0.96	8119	7307	5726
3016_03	0.94	6934	6240	4361
4297_01	0.97	7579	6821	6638
4297_02	0.70	4059	3653	3638
4297_05	0.88	7723	6950	4881
3121_01	0.66	7715	6944	3894
3121_03	0.95	8485	7636	5855
3121_04	0.86	8135	7322	6307

Table 4.2: Table shows the coefficients of determination, the initial number of points of the DIC data sets and the points filtered and compared. For each sample, the data are averaged on four repetitions.

In order to verify the goodness of fit, in the table 4.3 the results of the residual analysis are reported. In all the cases, with the exception of 3121_01, the residuals are included within 18% in correspondence of the 90% of the cumulative error function. In the figure 4.3 the residuals distribution and the cumulative error function are represented.

Sample	**Cumulative error function**			
	80%	**85%**	**90%**	**95%**
3029_01	11.41%	13.60%	17.03%	23.48%
3029_02	13.89%	15.52%	17.64%	19.71%
3029_03	6.96%	7.74%	8.88%	11.51%
3029_04	4.85%	5.49%	6.26%	7.55%
3029_05	2.28%	2.61%	3.13%	4.37%
3016_03	8.53%	10.00%	12.38%	14.92%
4297_01	1.68%	1.93%	2.34%	3.28%
4297_02	4.55%	5.16%	6.25%	8.10%
4297_05	10.87%	11.78%	13.02%	14.94%
3121_01	14.76%	17.49%	21.84%	41.03%
3121_03	3.74%	4.39%	5.15%	6.24%
3121_04	5.01%	5.35%	5.79%	6.51%

Table 4.3: The residuals calculated in corrispondence of 80%, 85%, 90% and 95% of the cumulative error function are reported.

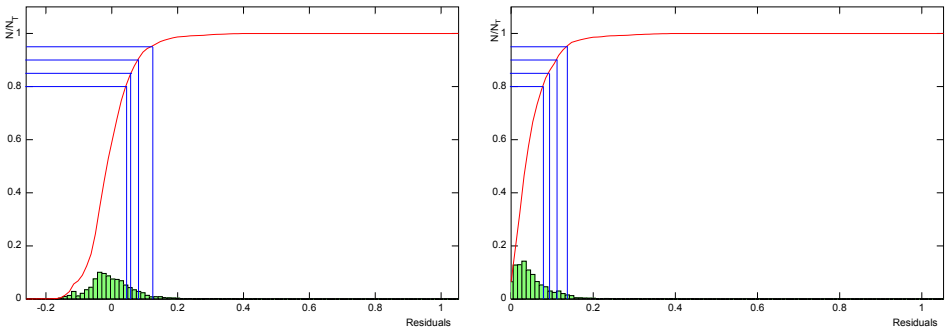

(a) (b)

Figure 4.3: The images show the residual analysis for the sample 3016_03. The absolute values of the residuals are reported, while in red the cumulative error function is represented and the considered values (80%,85%,90%,95%) are identified with blue lines.

4.2.2 Tissue elastic modulus

The tissue elastic modulus (E_t) evaluated as reported in chapter 3, were compared with extensometer-based method (where the values of $E_t^{ext,m}$ are evaluated as the mean value of the tissue elastic modulus calculated in the four repetition).

Analysing the results reported in the figure 4.5, it is notable that in all the sample of the first donor (3020_ 09) the estimations obtained with the traditional method ($E_t^{ext,m}$) and DIC one (E_t^{DIC}) are coherent. Moreover, globally there is coherence between the values estimated as E_t^{DIC} and with the extensometer on the same aspect $E_t^{ext,s}$. The same considerations can stem from the sample 4297_01 that is characterized by coherent value of E_t^{DIC} and $E_t^{ext,m}$.

Sample	BV/TV	Heterogeneity index %
3029_01	19.48	0.22
3029_02	15.84	0.44
3029_03	13.94	0.01
3029_04	21.43	0.21
3029_05	29.44	0.08
3016_03	12.43	0.01
4297_01	27.07	0.11
4297_02	23.16	0.36
4297_05	23.60	0.13
3121_01	12.90	0.30
3121_03	17.95	0.06
3121_04	17.03	0.02

Table 4.4: The BV/TV parameters are reported, evaluated as the mean values of the BV/TV between the upper and lower dataset acquired. The heterogeneity index is calculated as the percentage variation among the two data sets for each sample

Evaluating the other 6 specimens, two particular situation must be reported. In the first case, for two samples (4297_05 and 3121_01) the estimations of E_t^{DIC} and $E_t^{ext,s}$ are coherent, while $E_t^{ext,m}$ are significantly different. However, these measures are characterized by a high standard deviation, where DIC and extensometer estimations constituting the lower limit of this range due to a presumable high heterogeneity of the trabecular structure.

In the last four samples (3121_ 03, 3121_ 04, 3016_03 and 4297_02) the estimation over the single aspect of the cylinder, $E_t^{ext,s}$, is included in the range of standard deviation of the estimation obtained with the extensometer

on all the repetitions, $E_t^{ext,m}$. In these cases E_t^{DIC} underestimate the values of the extensometers and these would be linked to the DIC acquisition system. In fact, applying a stochastic pattern with dots of nominal dimension is a hard task for two main reasons:

- it is difficult to create a heterogeneous pattern especially for the considered dimensions;
- the DIC parameters are chosen considering the nominal dimensions of the pattern, but there was not a method to check the real dimensions.

Moreover, DIC system was developed to recognize displacements over a plane surface of a homogeneous object with a displacements in the order of *mm*. On the other hand trabecular bone specimens are characterized by a heterogeneous porous material, cylindrical shape and displacements registered in the order of μm. In particular further information are collected for some specimens. For sample 3016_03, the results show that the difference among E_t^{DIC} and $E_t^{ext,m}$ is included within 11%, moreover $E_t^{ext,m}$ registers a high standard deviation and E_t^{DIC} estimation is included in this range. Investigating on the difference registered with the estimation of $E_t^{ext,s}$ on the same aspect of the DIC acquisition, some consideration can be stem from the micro-structural parameters. In table 4.4 are reported the values of the BV/TV estimated on the two data sets acquired with the μCT (further information are reported in the chapter 2), and it results that this specimen has an homogeneous structure but it is characterized by the lower value of these indexes. This is confirmed by the figure 4.4 that shows the weak bone structure of the specimen. For the samples 4297_02 and 3121_01 a low correlation was registered between FEM and DIC displacements (as reported in table 4.2). While for the 3121_01 it was explained that measurement errors could be linked to the porous structure, for the sample 4297_02 further studies must be developed in order to improve all the steps of this procedure.

Overall, all the results, except for two samples, show a high correlation and the tissue elastic modulus obtained with the different methods are related.

4.3 Sensitivity studies

In order to evaluate the sensitivity of the results to assess the robustness of the method on varying the parameters used, several analysis were conducted. Two main categories of the sensitivity studies were individuated:

1 Analysis of the parameters used in the algorithms developed, that are:

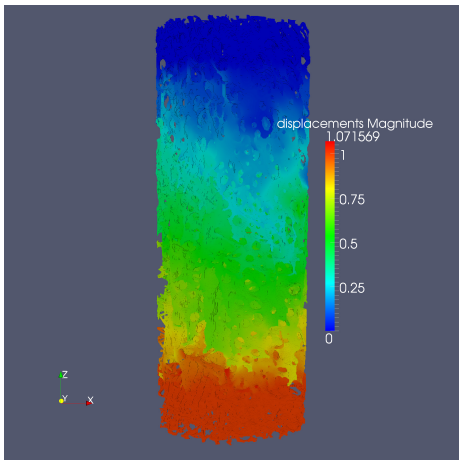

Figure 4.4: Sample 3016: the weak structure is covered by some trabecule that are hung to the structure, and some inhomogeneity can be noted on the displacements field. The color bar displayed how the displacements are distributed over the sample (in the order of mm) and this particular structure slides over the volume, causing the overlay of regions with different displacements.

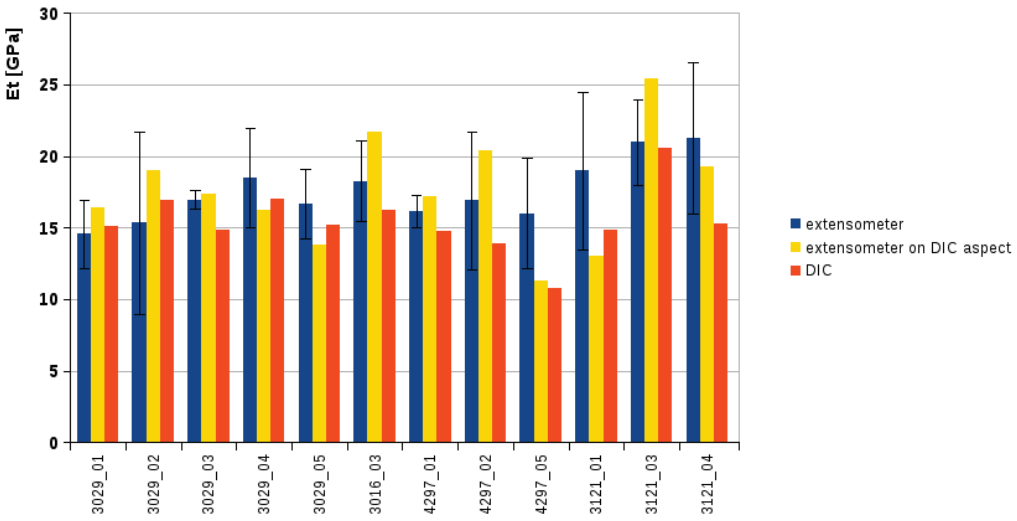

Figure 4.5: The bar chart shows for each sample the value of E_t evaluated with: the DIC-based method (E_t^{DIC}), the extensometer on four repetition $E_t^{ext,m}$ and the extensometer on same aspect acquired by the DIC $E_t^{ext,s}$.

- shell thickness;
- percentile used to filter DIC displacements field;
- area projected on the FEM data set for the displacements comparison between DIC and FEM point clouds.

2 Evaluation of the intrinsic parameters of DIC system, that are:

- facet step;
- facet size.

While the goal of the first analysis was to evaluate the parameters set chosen, the second one was to investigate whether the adopted set of parameter was appropriate for this particular work.
The procedure, described in the chapter 3, was performed applying different parameters and the correlation coefficient between DIC and FEM point sets are evaluated. Moreover, to estimate the goodness of fit, a residual analysis was performed and the percentage of residuals included until different values (80%, 85%, 90%, 95%) of the cumulative error function are considered. Each test was performed on the four repetition acquired for each sample.

4.3.1 Sensitivity on algorithms parameters

FEM thickness

In order to reduce the computational costs an external layer was extracted from the entire FEM volume. Due to the porosity of the specimens, there are not available algorithms to easily detect the most superficial points, so an angular portion of the models was picked. This is characterized by the same height of the original model, an angle is selected in order to obtain an external surface similar to the DIC points cloud, and a thickness is chosen to extract all the information available on the specimens surface. So it was investigated the sensitivity of the results to different thickness value, considering 0.5 mm, 0.9 mm, 1.2 mm, 1.5 mm. Then coefficients of determination R^2 and the residuals were evaluated, and the results are reported in the table 4.5:

Graph 4.6 shows the mean of the residuals obtained on the four repetition of a sample, calculated with different shell thickness.

DIC filtering

Once the points cloud was obtained, the displacements field had to be filtered to eliminate the vectors with components out of ordinary. The procedure

Shell thickness	R^2	Cumulative error function			
		80%	85%	90%	95%
0.5 mm	0.88	10.42%	11.30%	12.47%	14.29%
0.9 mm	0.88	10.67%	11.65%	12.91%	14.81%
1.2 mm	0.88	11.09%	12.15%	13.41%	15.46%
1.5 mm	0.88	11.28%	12.35%	13.67%	15.70%

Table 4.5: The table shows the coefficients of determination R^2 of FEM and DIC displacements in the direction of the cylinder axis. and the residuals to 80%, 85%, 90% and 95% of the cumulative error function are reported.

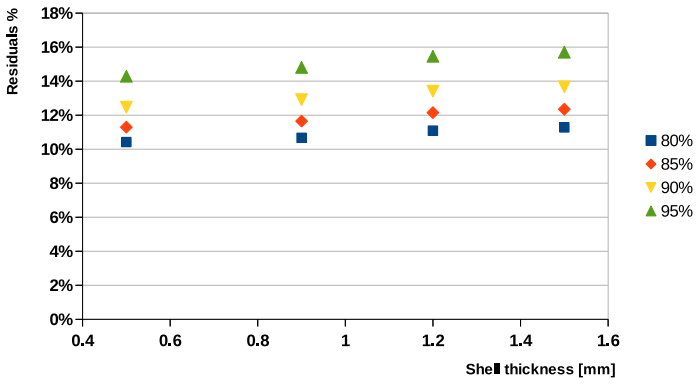

Figure 4.6: The graph shows the residuals, calculated with several shell thickness, which correspond to different percentage of the cumulative error function as reported in the legend (80% 85% 90% 95%).

developed allows to evaluate the angle included between vectors and the symmetry axis of the cylinder. The distribution of the angles was considered and a threshold value was applied excluding a percentile of the distribution. The threshold value was evaluated considering several percentiles (70th, 75th, 80th, 85th, 90th, 95th) and the correlation between DIC and numerical model was considered on varying of these parameters.
Tables 4.6 show the correlation coefficients and residuals for four specimens and the trends are reported in the figures 4.7 4.8 4.9 4.10.

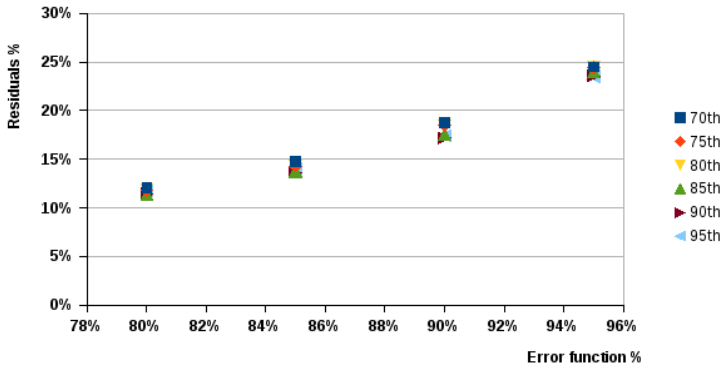

Figure 4.7: Graph shows the residuals trends of the sample 3029 01 for each percentile reported in the key. Specimen is indicated with the identification number used in the laboratory.

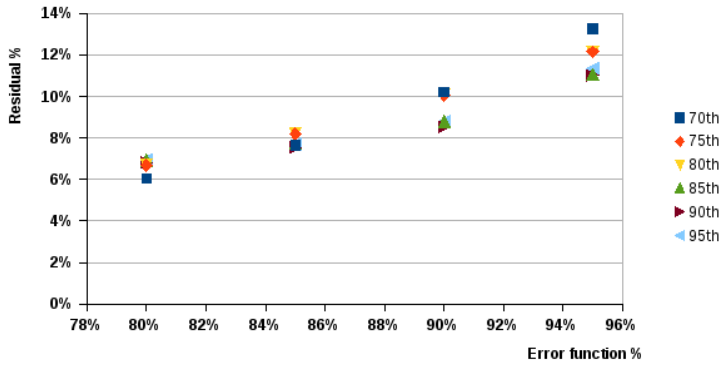

Figure 4.8: Graph shows the residuals trends of the sample 3029 03 for each percentile reported in the key. Specimen is indicated with the identification number used in the laboratory.

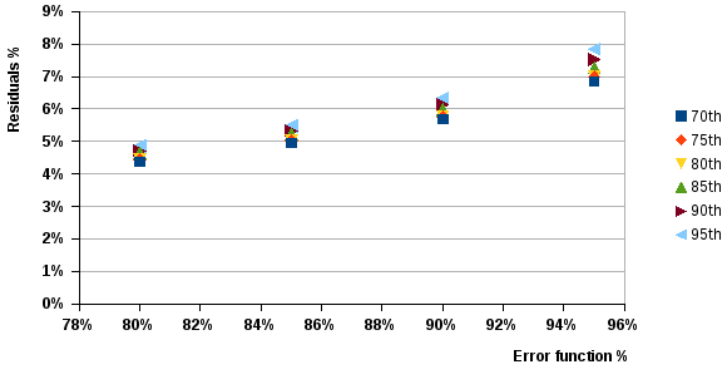

Figure 4.9: Graph shows the residuals trends of the sample 3029 04 for each percentile reported in the key. Specimen is indicated with the identification number used in the laboratory.

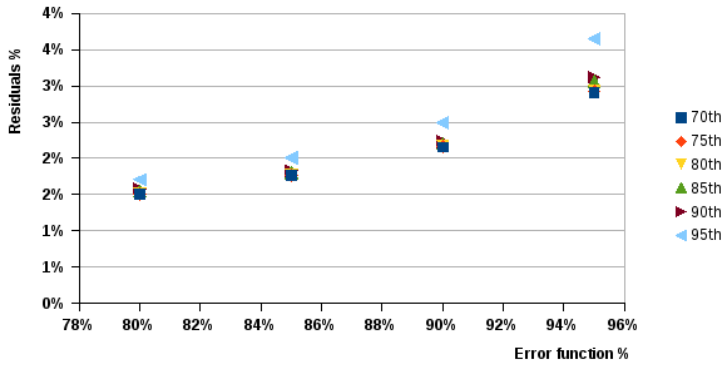

Figure 4.10: Graph shows the residuals trends of the sample 4297 01 for each percentile reported in the key. Specimen is indicated with the identification number used in the laboratory.

Specimen	Percentile	R^2	Cumulative error function			
			80%	**85**%	**90**%	**95**%
3029 01	70th	0.90	12.08%	14.76%	18.80%	24.49%
	75th	0.91	11.83%	14.29%	18.45%	24.44%
	80th	0.92	11.83%	14.29%	18.45%	24.44%
	85th	0.92	11.39%	13.73%	17.51%	24.00%
	90th	0.93	11.43%	13.65%	17.17%	23.56%
	95th	0.93	11.78%	13.99%	17.40%	23.55%
3029 03	70th	0.94	6.06%	7.64%	10.21%	13.28%
	75th	0.95	6.68%	8.18%	10.07%	12.15%
	80th	0.95	6.68%	8.18%	10.07%	12.15%
	85th	0.95	6.93%	7.75%	8.80%	11.05%
	90th	0.95	6.83%	7.55%	8.54%	11.00%
	95th	0.95	6.97%	7.70%	8.81%	11.34%
3029 04	70th	0.98	4.37%	4.95%	5.69%	6.84%
	75th	0.98	4.43%	5.01%	5.76%	6.99%
	80th	0.98	4.43%	5.01%	5.76%	6.99%
	85th	0.98	4.62%	5.21%	5.98%	7.27%
	90th	0.97	4.72%	5.33%	6.13%	7.52%
	95th	0.97	4.85%	5.48%	6.34%	7.84%
4297 01	70th	0.98	1.50%	1.76%	2.16%	2.91%
	75th	0.98	1.51%	1.76%	2.16%	2.93%
	80th	0.98	1.51%	1.76%	2.16%	2.93%
	85th	0.98	1.55%	1.80%	2.20%	3.06%
	90th	0.97	1.58%	1.83%	2.23%	3.12%
	95th	0.96	1.71%	2.01%	2.49%	3.65%

Table 4.6: Table shows correlation coefficients and residuals for four samples on varying the percentile excluded from the distribution. The specimens are indicated with the identification number used in the laboratory.

Area projected on FE models

In order to compare DIC and FEM displacements, each DIC point was projected over the FEM shell and the correspondent surrounding volume is selected. The dimensions of this volume are evaluated considering the distance between DIC points, which is referred as facet step. The volume is a square prism and referring to the figure 4.11, the side dimension l of the square area is investigated. The sensitivity of the results to different dimension of the sur-

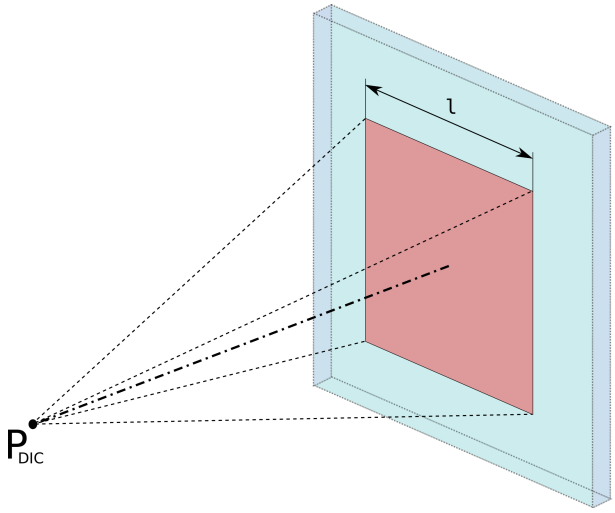

Figure 4.11: Projection of DIC point on FE model. As referred in the figure, l represents the side dimension of the square area considered.

faces were investigated considering three values for the side dimension: 0.075 mm, 0.1 mm, 0.15 mm. The table 4.7 shows coefficients of determination R^2 and residuals on varying these parameters.

Side dimension [mm]	R^2	**Cumulative error function**			
		80%	**85%**	**90%**	**95%**
0.075	0.88	10.74%	11.73%	12.98%	14.90%
0.1	0.88	10.72%	11.72%	12.95%	14.89%
0.15	0.89	10.70%	11.68%	12.94%	14.90%

Table 4.7: Table shows the coefficients of determination R^2 and the residuals on varying the comparing area.

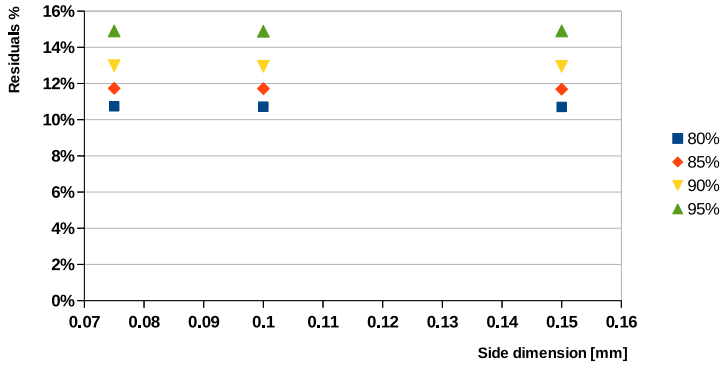

Figure 4.12: Graph shows the residuals which correspond to different percentage of the cumulative error function (80% 85% 90% 95%) on varying side dimension of the area considered for the comparison between DIC and FEM point clouds.

4.3.2 Sensitivity on DIC intrinsic parameters

Facet size and facet step

Two parameters related to DIC acquisition are set: facet size and facet step, while the overlap between two facet is computed automatically from the system. The frames were acquired with a set up assessed in a previous study [27], but it was not verified for trabecular bone specimens. In fact, for the particular micro structure of this kind of bone, it was necessary to examine the setting for system acquisition. Moreover, this is the first time in which FE models and DIC frames are compared, so the used layout was not developed for this specific application and the sensitivity of the results on varying the setting are considered. So two different analysis are conducted, the first one maintaining the facet size fixed and varying the facet step, the second mantaining the facet step fixed and varying the facet size. The considered values are reported in table 4.8.

The coefficients of determination R^2 of the regression among DIC and FEM displacements was calculated and also a residual analysis was performed in order to evaluate the goodness of fit. The table 4.9 and graph 4.13 show the results obtained with the step size fixed, while the table 4.10 and the graph 4.14 show the coefficients of determination R^2 and the residuals varying the facet step.

	Facet size [pixel]	Facet step [pixel]	Overlap %
Fixed facet step	10	10	0%
	20		50%
	35		71%
	50		80%
Fixed facet size	35	5	86%
		10	71%
		15	57%

Table 4.8: Tables show the parameters set up used in these sensitivity tests.

Facet size [pixel]	R^2	Cumulative error function			
		80%	**85%**	**90%**	**95%**
10	0.90	9.53%	10.66%	12.03%	14.25%
20	0.88	10.98%	12.13%	13.41%	15.32%
35	0.88	10.81%	11.76%	13.01%	15.02%
50	0.90	9.40%	10.29%	11.53%	13.60%

Table 4.9: Table shows the coefficients of determination R^2 and the residuals obtained varying the facet size. The residuals were evaluated at the following percentage of the cumulative error function: 80%, 85%, 90%, 95%.

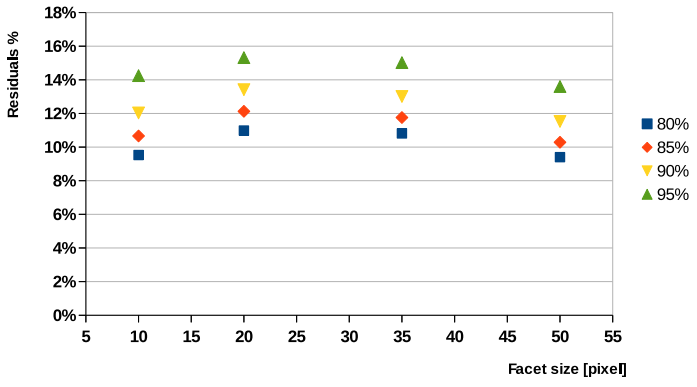

Figure 4.13: The graph shows the residuals correspondent to different percentage of the cumulative error function (80% 85% 90% 95%), considering the step size fixed and facet step of 10 pixel.

Facet step [pixel]	R^2	**Cumulative error function**			
		80%	**85%**	**90%**	**95%**
5	0.90	10.61%	11.64%	12.87%	14.76%
10	0.88	10.81%	11.76%	13.01%	15.02%
15	0.88	10.52%	11.57%	12.81%	14.69%

Table 4.10: Table shows the results obtained varying the facet step with the facet size fixed to 35 pixel

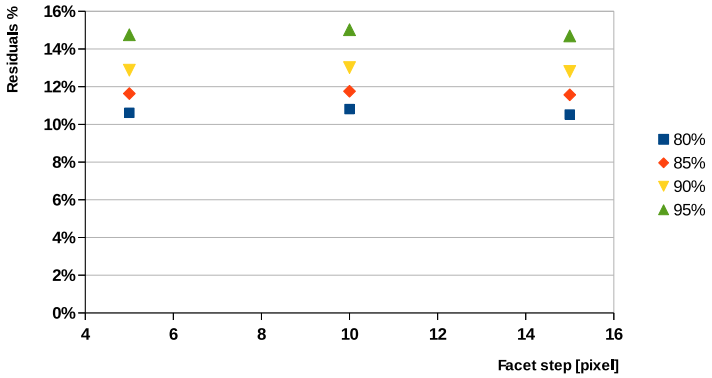

Figure 4.14: The graph shows the residuals which correspond to different percentage of the cumulative error function (80% 85% 90% 95%) with a facet size of 35 pixel and on varying the facet step.

4.4 Discussion

The aim of the sensitivity studies was twofold: to evaluate how the results are influenced by the parameters chosen in the developed algorithms and to assess the intrinsic parameters used during the DIC acquisition.
The first analysis concerned the thickness extracted from the FE models. The results reported in the table 4.5 seems to confirm what was expected: on varying the shell thickness there are not variation in the coefficient of determination. Moreover the residuals analysis shown that around 13% of the residuals are included in the 90% of the population and around 15% in the 95% of the population in all the cases considered. Thus the results are not influenced by a different shell thickness, so the choice of $0.9mm$ is acceptable.

In the table 4.6 is notable that there is not a significant variation between the coefficient of determination on varying the percentile. Evaluating the trends of residuals for each specimen, there are not notable differences within 90% while to 95% the residuals deeply increase. There is not a significant difference between the percentile tested, but choosing low percentile imply that a large amount of points are excluded. So the choice to select 90th of points is a compromise in order to maintain more information.

The dimension of the area projected on the FE models were chosen considering the distance between DIC points. In this test, the sensitivity of the results to different side dimension are considered and in the table 4.7 are shown the coefficients of determination and the residuals. There are not significant difference in ^{2} on varying the dimension, and the residuals within the 90% are included by 12.89%. Thus this test confirms the choice of 0.05 mm is not critical

The last case investigated does not concern the parameters implied in the developed algorithms, but it was a study to assess the method used to acquire DIC frames of trabecular bone for comparison with FE models. The first test examines the sensitivity to different facet size, while the second one evaluates the sensitivity on varying the facet step. The tables 4.10 and 4.9 show that there are not significant difference in R^2 and the residuals are included around 13% in both the tests. These results validate the setting used to acquire the frames (facet size = 35 pixel and facet step = 10 pixel). Then, the sensitivity studies confirm that no critical result is connected with a variation of numerical as well as experimental settings, for this reason the adopted parameter can be considered acceptable.

Chapter 5

Conclusion

A significant social and economic problem is linked to age-related bone fracture. Due to the increasingly ageing population the age-related bone fractures cover a relevant cost each year, so several studies are focused on the research of strategies for prevention and treatment. A typical research question is to accurately predict the bone fracture risk. There are two main reasons that influences the fracture risk: the loads distribution and the intrinsic features that are structure and material proprieties. The first step to develop predictive bone models is to understand the mechanisms that influence the bone mechanical quality and proprieties.
In this research context, at the Rizzoli Orthopaedic Institute, the attention was focused on the investigation of the human trabecular bone proprieties at tissue level. The adopted technique is based on the combination of experimental test and numerical model based on μFEM which are derived from μCT data set. In the experimental test the apparent elastic modulus E_{app}^{EXP} is assessed though an uni-axial compressive test; then the tissue elastic modulus E_t are estimated combining E_{app}^{EXP} and E_{app}^{FEM} obtained from the numerical model.
Cancellous bone is characterized by a porous and heterogeneous structure which causes several difficulties to accurately estimate the mechanical proprieties. The experimental test is based on the measurements of the displacements over the bone surface with an extensometer, whose knives are inserted on the structure surface. Thus, this instrument performs a punctual measure related to a restricted contact area between the instrument and the sample. Moreover, the experimental layout requires that the bone specimen extremities are inserted in two end cups and bond with PMMA cement. The mechanical behaviour of these elements can not be fully controlled, and due to possible residual plays between the specimens and the end cups it is a hard task to estimate the real displacements that are applied on the bone spec-

imens. The numerical models are based on the following assumptions: (i) the accurate reproduction of the bone structure based on the μCT imaging, (ii) the tissue elastic modulus E_t does not vary on the dimension of a sample scale, (iii) the idealized boundary conditions. These assumptions permit an exact description of the physical system to estimate the tissue elastic modulus E_t. Since all the experimental measures are used to estimate E_t, there are not independent measures to perform a validation of the FEM modelling.
To overcome these limits a new method was recently adopted: the Digital Image Correlation (DIC) that allows to obtain a 3D points set and the related displacements field of a whole portion of sample surface.
Aim of this work was twofold: first at all evaluate the coherence between the displacements fields obtained with numerical models and that resulting from DIC acquisitions. Then the tissue elastic modulus was evaluated combining the experimental measurements performed using the DIC displacements monitoring and the data extracted by the FE models.
FEM and DIC point sets are obtained from two different procedures and for this reason they are characterized by different features. FE models represent the whole volume of bone specimens and the resolution is 39 μm, which was obtained from μCT imaging. Conversely, DIC data sets represent only the superficial points of one aspect of the cylindrical sample and the distance between the points acquired by means of optical facilities is 100μm. Moreover, due to the the dimensions and structural proprieties of trabecular bone samples, the DIC acquisitions are subjected to different factors that may significantly affect the accuracy of the displacement fields. In this particular application, due to the technological limits of the available facilities, the limited dimensions of the sample as well as the non-continuum nature of the external surfaces may cause a significant lack of accuracy in some cases.
The data sets were elaborated and an accurate and totally automatic procedure was developed to register numerical model and DIC points cloud of trabecular bone specimens. Finally, a strategy was developed to compare the displacement fields.
Experimental tests were performed on 20 specimens, which were extracted from four donors. Among these samples, only 12 specimens resulted adequate for the aim of this study. For each sample, the regression analysis performed for each experimental repetition demonstrated a high correlation (R^2 in the range of 0.84-0.97) between the FEM and DIC displacement fields. The residual analysis showed the goodness of the conformity of the two displacement fields (90% of the residuals distributed within the 17.6%; 95% of the residuals distributed within the 23%). The assessed value of the tissue elastic modulus obtained with DIC method and the traditional method, based on the extensometer, were compared. In both cases, the E_t values

resulted aligned with that reported in literature for the human trabecular bone. The differences resulted between these sets of values were included within 15%. Two cases presented a low correlation between displacement fields; three cases presented a considerable difference among the elastic modulus E_t; among these five cases, one presented both the low correlation and considerable difference among the elastic modulus. In some cases it was demonstrated that these results could be related to the lack of consistence of the trabecular structure over the surface acquired by DIC system. In the remaining cases some considerations stemmed from the setting and technology of DIC system: in fact, the layout developed for the DIC acquisition was not optimized for this particular application and for these reasons several studies are being conducted to improve the setting conditions in order to minimise the noise improving the reliability of DIC measurements.
Finally, sensitivity studies were conducted to assess the robustness of the method on varying the used parameters. The influences of the parameters chosen in the developed algorithms and the setting of the DIC system were investigated. No critical values were found: the coefficient of determination (R^2 resulted in all the cases between 0.88 and 0.98), and the residual analysis confirmed the goodness of fit (considering 90% of the points set, the residuals are included within 18%).

This work was focused on the development and evaluation of a robust and accurate procedure to compare DIC and FEM displacement fields. The results show all the potentiality of the Digital Image Correlation and this method would pave the ways for a new procedure, more accurate than the extensometer-based, to evaluate the tissue elastic modulus for trabecular bone specimens. Finally, this technique could allow a validation of the numerical models the which is a mandatory step in the clinical application perspective.

Appendix A

Cylindrical fitting

In this appendix an analytical solution for the cylindrical fitting is presented [13]. An infinite cylinder with an axis **D**, point **C** on the axis, and radius **r** >0 is defined implicitly by:

$$(X - C)^T (I - DD^T)(X - C) = r^2 \tag{A.1}$$

So there are seven parameter to evaluate: r, three component for C and three component for D.

The height direction is assumed to be $U = (0, 1, 0)$, so $D = (d_0, 0, d_2)$. A right vector is defined as $R = U \times D = (d_2, 0, -d_0)$. The data is assumed to be approximately distributed over a convex domain, "arranged as a rectangle in the planes x-z". Considering P_i the samples, let **A** be the average of the samples,

$$A = \frac{1}{n} \sum_{i=0}^{n-1} P_i \tag{A.2}$$

In order to make the numerical computations robust, the average is subtracted from the sample.

$$Q_i = P_i - A \tag{A.3}$$

The cylinder axis $D = (d_0, 0, d_2)$ is estimated by fitting a line to the projections of the Q_i onto the xz-plane. The covariance matrix M of the projections is defined as:

$$\begin{bmatrix} \sum_{i=0}^{n-1} x_i^2 & \sum_{i=0}^{n-1} x_i z_i \\ \sum_{i=0}^{n-1} x_i z_i & \sum_{i=0}^{n-1} z_i^2 \end{bmatrix} \tag{A.4}$$

Factor the matrix as $M = RMR^T$, where R is a rotation matrix whose coloumns are the eigenvectors and where D is a diagonal matrix whose diagonal terms are the eigenvalues. The cylinder direction has D_0 equal to $R(0, 1)$ and D_2 equal to $R(1, 1)$.

Define $x_i = R \cdot Q_i$ and $y_i = U \cdot Q_i$, we want to fit the points (x_i, y_i) with a circle whose centre is c and radius r. The circle is defined by :

$$x^2 + (y - c)^2 - r^2 = 0 \tag{A.5}$$

Define the error function:

$$E(c, r) = \sum_{i=0}^{n-1} [x_i^2 + (y_i - c)^2 - r^2]^2 \tag{A.6}$$

If all the points lie on a circle, we should obtain c and r for which $E(c, r) = 0$. However, the points will not lie on a circle, so the best we can do is compute c and r that minimise $E(c, r)$. The minimum occur when the partial derivatives A.7 of E are zero:

$$\begin{aligned} \frac{\partial E}{\partial r} &= -4 \sum_{i=0}^{n-1} [x_i^2 + (y_i - c)^2 - r^2] r, \\ \frac{\partial E}{\partial c} &= -4 \sum_{i=0}^{n-1} [x_i^2 + (y_i - c)^2 - r^2](y_i - c) \end{aligned} \tag{A.7}$$

These form a linear system of equations A.8.

$$\begin{bmatrix} n & \sum_{i=0}^{n-1} y_i \\ \sum_{i=0}^{n-1} y_i & \sum_{i=0}^{n-1} y_i^2 \end{bmatrix} \begin{bmatrix} r^2 - c \\ 2 \cdot c \end{bmatrix} = \begin{bmatrix} \sum_{i=0}^{n-1} (x_i^2 + y_i^2) \\ \sum_{i=0}^{n-1} (x_i^2 + y_i^2) y_i \end{bmatrix} \tag{A.8}$$

Solving this system, the solution is given by the equation A.9.

$$\begin{bmatrix} r^2 - c \\ 2 \cdot c \end{bmatrix} = \begin{bmatrix} \sum_{i=0}^{n-1} y_i^2 & -\sum_{i=0}^{n-1} y_i \\ -\sum_{i=0}^{n-1} y_i & n \end{bmatrix} \begin{bmatrix} \sum_{i=0}^{n-1} (x_i^2 + y_i^2) \\ \sum_{i=0}^{n-1} (x_i^2 + y_i^2) y_i \end{bmatrix} \tag{A.9}$$

In the original coordinates of the sample points, the cylinder centre is:

$$C = A + (0, c, 0). \tag{A.10}$$

Appendix B

3-D linear regression

In this appendix the analytical solution of a 3-D Linear Least Squares Fitting is described [37].
Considering the points coordinates P_k, with k=1...n , the orthogonal projection of P_k on a straight line L is H_k and the perpendicular offset is $d_k = P_k H_k$. The fitting problem is to find L so that minimize $\sum_1^n d_k^2$. The plane Π, perpendicular to the line L, containing the origin (0, 0, 0) has the following equation:

$$z = ax + by \tag{B.1}$$

and the line L which intersects the plane Π in a point H(u, v, w) has the following equation:

$$w = au + bv \tag{B.2}$$

In order to find the equation of line L, the four coefficients(a, b, u, v) have to be calculated, as function of the points coordinates X_k, Y_k and Z_k (k=1, ..., n). The orthogonal projection of the point $P_k(X_k, Y_k, Z_k)$ on the plane π is p_k (x_k, y_k, z_k), where:

$$z_k = ax_k + by_k \tag{B.3}$$

x_k, y_k, z_k can be expressed as function of X_k, Y_k, Z_k, considering the distance between P_k and p_k:

$$d^2 = (x_k - X_k)^2 + (y_k - Y_k)^2 + (z_k - Z_k)^2 \tag{B.4}$$

Using the equation B.3:

$$d^2 = (x_k - X_k)^2 + (y_k - Y_k)^2 + (ax_k + by_k - Z_k)^2 \tag{B.5}$$

In order to calculate the minimum distance of P_k to any point of π, this leads to the partial derivatives of this function of x_k and y_k:

$$\begin{aligned} \frac{\partial d^2}{x_k} &= (x_k - X_k) + a(ax_k + by_k - Z_k) = 0 \\ \frac{\partial d^2}{y_k} &= (y_k - Y_k) + b(ax_k + by_k - Z_k) = 0 \end{aligned} \tag{B.6}$$

x_k and y_k are extracted from the previous equation (eq:B.6), then from the eq.B.3 we obtain:

$$\begin{aligned} x_k &= [(1+b^2)X_k - abY_k + aZ_k](1+a^2+b^2)^{-1} \\ y_k &= [-abX_k + (1+a^2)Y_k + bZ_k](1+a^2+b^2)^{-1} \\ z_k &= [aX_k + bY_k + (a^2+b^2)Z_k](1+a^2+b^2)^{-1} \end{aligned} \tag{B.7}$$

The distance d_k of the point P_k to the regression line is:

$$d_k^2 = (x_k - u)^2 + (y_k - v)^2 + (z_k - w)^2 \tag{B.8}$$

substituing the equation B.2, the sum of the squares of the distances for the set of n points is:

$$\sum d_k^2 = \sum (x_k - u)^2 + \sum (y_k - v)^2 + \sum (z_k - au - bv)^2 \tag{B.9}$$

To find the minimum of $\sum d^2$, the partial derivative are considered:

$$\begin{aligned} \frac{\partial(\sum d_k^2)}{2\partial u} &= -\sum (x_k - u) - a\sum z_k - au - bv = 0 \\ \frac{\partial(\sum d_k^2)}{2\partial v} &= -\sum (y_k - v) - b\sum z_k - au - bv = 0 \\ \frac{\partial(\sum d^2)}{2\partial a} &= \sum (x_k - u)\frac{\partial x_k}{\partial a} + \sum (y_k - v)\frac{\partial y_k}{\partial a} + \\ &\quad \sum z_k - au - bv(\frac{\partial z_k}{\partial a} - u) = 0 \\ \frac{\partial(\sum d^2)}{2\partial b} &= \sum (x_k - u)\frac{\partial x_k}{\partial b} + \sum (y_k - v)\frac{\partial y_k}{\partial b} + \\ &\quad \sum z_k - au - bv(\frac{\partial z_k}{\partial b} - v) = 0 \end{aligned} \tag{B.10}$$

The equations B.9 and B.10 can be rewritten as:

$$\begin{aligned} n(1+a^2u) + nabv &= \sum x_k + a\sum z_k \\ nabu + n(1+b^2)v &= \sum y_k + b\sum z_k \end{aligned} \tag{B.11}$$

Substituting in the equation B.2 $\sum x_k$, $\sum y_k$ and $\sum z_k$ to x_k, y_k, z_k, after some factorization the parameters u,v, and w can be expressed as:

$$u = \frac{1}{1+a^2+b^2}\left[(1+b^2)\frac{1}{n}\sum x_k - ab\frac{1}{n}\sum y_k + a\frac{1}{n}\sum z_k\right] \tag{B.12}$$

$$v = \frac{1}{1+a^2+b^2}\left[-ab\frac{1}{n}\sum x_k + (1+a^2)\frac{1}{n}\sum y_k + b\frac{1}{n}\sum z_k)\right] \tag{B.13}$$

$$w = \frac{1}{1+a^2+b^2}\left[a\frac{1}{n}\sum x_k + b\frac{1}{n}\sum y_k + (a^2+b^2)\frac{1}{n}\sum z_k\right] \tag{B.14}$$

In order to simplify the demonstration, the following notation is used:

$$\begin{aligned}
S_{xx} &= \frac{1}{n}\sum X_k^2 - \left[\frac{1}{n}\sum X_k\right]^2 \\
S_{yy} &= \frac{1}{n}\sum Y_k^2 - \left[\frac{1}{n}\sum Y_k\right]^2 \\
S_{zz} &= \frac{1}{n}\sum Z_k^2 - \left[\frac{1}{n}\sum Z_k\right]^2 \\
S_{xy} &= \frac{1}{n}\sum X_k^2 Y_k^2 - \frac{1}{n^2}\sum X_k \sum Y_k \\
S_{yz} &= \frac{1}{n}\sum Y_k^2 Z_k^2 - \frac{1}{n^2}\sum Y_k \sum Z_k \\
S_{xz} &= \frac{1}{n}\sum Y_k^2 Z_k^2 - \frac{1}{n^2}\sum X_k \sum Z_k
\end{aligned} \tag{B.15}$$

Pluggin the equations B.7 and B.12,B.13,B.14 in the equation B.9 and using the notation previously described B.15, we obtain:

$$\sum d_k^2 = \frac{n}{1+a^2+b^2}$$

$$\left[(1+b^2)S_{xx} + (1+a^2)S_{yy} + (a^2+b^2)S_{zz} - 2abS_{xy} + 2aS_{xz} + 2bS_{yz}\right] \tag{B.16}$$

Defining:

$$\delta_m = \sqrt{\frac{1}{n}\sum d_k^2} \tag{B.17}$$

The equation B.16 is a quadratic relationship between a and b and can be rewritten as:

$$C_{11}a^2 + C_{22}b^2 + 2C_{12}ab + 2C_{10}a + 2C_{01}b + C_{00} = 0 \tag{B.18}$$

where the coefficients are defined as:

$$\begin{aligned} C_{11} &= S_{yy} + S_{zz} - \delta_m \\ C_{22} &= S_{xx} + S_{zz} - \delta_m \\ C_{12} &= -S_{xy} \\ C_{10} &= S_{xz} \\ C_{01} &= S_{yz} \\ C_{00} &= S_{xx} + S_{yy} - \delta_m \end{aligned} \tag{B.19}$$

So we can map the deviation δ_m as a family of ellipses and in order to eliminate a and b from the equation the following equation can be written to find the centre of the ellipses :

$$\begin{aligned} A &= a\cos\theta + b\sin\theta \\ B &= -a\sin\theta + b\cos\theta \end{aligned} \tag{B.20}$$

Substituting in the equation B.18 the terms reported in B.19 and B.20, we obtain:

$$\begin{aligned} (K_{11} - \delta_m^2)A^2 + (K_{22} - \delta_m^2)B^2 + \\ 2K_{12}AB + 2K_{10}A + 2K_{01}B + (K_{00} - \delta_{m^2}) = 0 \end{aligned} \tag{B.21}$$

where the coefficients are defined as:

$$\begin{aligned} K_{11} &= (S_{yy} + S_{zz})\cos^2\theta + (S_{xx} + S_{zz})\sin^2\theta - 2S_{xy}\cos\theta\sin\theta \\ K_{22} &= (S_{yy} + S_{zz})\sin^2\theta + (S_{xx} + S_{zz})\cos^2\theta - 2S_{xy}\cos\theta\sin\theta \\ K_{12} &= -S_{xy}(\cos^2\theta - \sin^2\theta) + (S_{xx} + S_{yy})\sin\theta + \cos\theta \\ K_{10} &= S_{xz}\cos\theta + S_{yz}\sin\theta \\ K_{01} &= -S_{xz}\sin\theta + S_{yz}\cos\theta \\ K_{00} &= S_{00} + S_{yy} \end{aligned} \tag{B.22}$$

Imposing K_{12}=0 and rewriting the equation B.21, we obtain that the ellipse collapse on a point when:

$$\frac{K_{10}^2}{K_{11} - \delta_m^2} + \frac{K_{01}^2}{K_{22} - \delta_m^2} - K_{00} + \delta_m^2 = 0 \tag{B.23}$$

Then the minimum of δ_m will be computed solving the following equation:

$$\left(\delta_m^2\right)^3 + c_2\left(\delta_m^2\right)^2 + c_1\left(\delta_m^2\right) + c_0 = 0 \tag{B.24}$$

and the coefficients are:

$$\begin{aligned} c_2 &= -K_{00} - K_{11} - K_{22} \\ c_1 &= K_{00}K_{11} + K_{00}K_{11} + K_{11}K_{22} - K_{01}^2 - K_{10}^2 \\ c_0 &= K_{01}^2K_{11} + K_{10}^2K_{22} - K_{00}K_{11}K_{22} \end{aligned} \tag{B.25}$$

Then solving the cubic equation B.23, with the smallest value δ_m, and defining

$$X_m = \frac{1}{n}\sum X_k;\ Y_m = \frac{1}{n}\sum Y_k;\ Z_m = \frac{1}{n}\sum Z_k; \tag{B.26}$$

the solution is achieved as:

$$\begin{aligned}
a &= \frac{-K_{10}}{K_{11}-\delta_m^2}\cos\theta + \frac{K_{01}}{K_{22}-\delta_m^2}\sin\theta \\
b &= \frac{-K_{10}}{K_{11}-\delta_m^2}\sin\theta + \frac{K_{01}}{K_{22}-\delta_m^2}\cos\theta \\
u &= \frac{1}{1+a^2+b^2}\left[(1+b^2)X_m - abY_m + aZ_m\right] \\
v &= \frac{1}{1+a^2+b^2}\left[-abX_m + (1+a^2)Y_m + bZ_m\right] \\
w &= \frac{1}{1+a^2+b^2}\left[aX_m - bY_m + (a^2+b^2)Z_m\right]
\end{aligned} \tag{B.27}$$

The exact value of a,b,u,v and w are known and the points H(u, v, w) and M(X_m, Y_m, Z_m) are defined. The regression line is the straight line which passes through the points H and M and is perpendicular to the plane $z = ax + by$.

Appendix C

Registration algorithms

In this appendix the main features of Iterative Closest Point and Trimmed Iterative Closest Point algorithms are given [5][9]. Given two 3D point sets, P with N_P points and M with N_M points, the ICP is composed by three main steps:

1. Each point of P and of M are paired together;

2. In order to minimize the mean square error (MSE) among the paired points, a geometrical transformation is calculated.

3. The optimal trasformation is applied and the MSE is updated.

The ICP algorithm is iterated until the value of MSE falls below a prefixed threshold [9].

In order to improve the robustness, speed and precision, different cost functions and minimization procedures are developed. Particularly, robust statistic can be applied such as Least Median of Squares (LMedS) or Least Trimmed Squares (LTS). These statistics are defined to robustify the standard Least Square technique and to make the process insensitive to outliers. With the purpose of explaining the difference among the three statistics, a linear regression model can be considered:

$$y_i = \beta_0 + \beta_1 x_{i1} + \cdots + \beta_m x_{im} + e_i \tag{C.1}$$

where $x_{i1}...x_{im}$ are the explanatory variables, β_j j=0,...,m the model parameters, y_i the response variables and e_i is assumed to have a gaussian distribution with zero mean.

In order to minimise the sum of squares of the residuals $r_i(\beta_0, \ldots, \beta_m)$, the variables β_j are computed with the following three statistics:

- Standard Least Square :

$$\underset{(\beta_0,\ldots,\beta_m)}{minimise} \sum_{(1:n)} r_i^2 \tag{C.2}$$

- Least Median Square:

$$\underset{(\beta_0,\ldots,\beta_m)}{minimise}\, med\, r_i^2 \tag{C.3}$$

- Least Trimmed Squares:

$$\underset{(\beta_0,\ldots,\beta_m)}{minimise} \sum_{(i:h)} (r_i^2)_{(1:n)} \tag{C.4}$$

where $r_{i_{i=1\ldots n}}$ indicates the ordered squared residual.

Actually LTS is preferred for its statical efficiency and it is less sensitive to local effects. In addiction the Trimmed Iterative Closest Points (TrICP) procedure, based on the consistent use of LTS approach, was developed. Considering two sets of 3D points, the data set P and the model M, the number of points in the two set is different (N_P and N_M), and a large portion of the data points may have no correspondence in the model set. Hypothesizing an euclidean motion, with rotation matrix R and translation vector t, the points of P overlaying on the dataset M, are defined as:

$$P = \{p_i(R,t)\}_{(i=1\ldots N_p)} \tag{C.5}$$

TrICP is composed by the following steps:

1. For each point p_i of P, find the closest point m_i of M and calculate the distance d_i^2:
$$d_i(R,t) = \|m_{cl}(i,R,t) - p_i(R,t)\|; \tag{C.6}$$
where m_{cl} is the individual distance from a data point $p_i(R,t)$ to the model set M evaluated as:
$$m_{cl}(i,R,t) = min\|m - p_i(R,t)\|, \tag{C.7}$$
.

2. Sort d_i^2 in the increasing order and calculate the LTS statistics as reported in the equation C.4.

3. Considering a stopping condition calculated as one of the following manner:

   - the maximum number of iteration N_{iter} has been reached;
   - the MSE is lower than a given tolerance;
   - the difference between MSE calculated on consecutive iteration, is lower than a given condition;

   if one of these breaking condition is satisfied, the iteration can be terminated.

4. Apply the optimal transformation found (R, t) to the pair of points.

5. Transform P according to (R, t).

According to *Chetverikov et al* [9], the optimal motion (R,t) is evaluated by the unit quaternion method due to Horn, which was considered the most robust. Although *Eggert et al* [15] described four efficient solutions to calculate transformation parameters. One of these algorithms is the Walker's technique which is the most significantly different of the four. In this method, dual quaternion is used to calculate the rotation matrix and translation, and it allows to evaluate simultaneous rotation and translation around a line in 3D space; the motion being defined by an angle θ and a distance t.

Bibliography

[1] Peter Arbenz, G Harry Van Lenthe, Uche Mennel, and M Ralph. Multi-level -Finite Element Analysis for Human Bone Structures. pages 1–10.

[2] Peter Arbenz, G.Harry Lenthe, Uche Mennel, Ralph Müller, and Marzio Sala. Multi-level μ-finite element analysis for human bone structures. In Bo Kå gström, Erik Elmroth, Jack Dongarra, and Jerzy Waśniewski, editors, *Applied Parallel Computing. State of the Art in Scientific Computing*, volume 4699 of *Lecture Notes in Computer Science*, pages 240–250. Springer Berlin Heidelberg, 2007.

[3] Peter Arbenz, G. Harry van Lenthe, Uche Mennel, Ralph Müller, and Marzio Sala. A scalable multi-level preconditioner for matrix-free μ-finite element analysis of human bone structures. *International Journal for Numerical Methods in Engineering*, 73(7):927–947, 2008.

[4] Harun H. Bayraktar, Elise F. Morgan, Glen L. Niebur, Grayson E. Morris, Eric K. Wong, and Tony M. Keaveny. Comparison of the elastic and yield properties of human femoral trabecular and cortical bone tissue. *Journal of Biomechanics*, 37(1):27–35, 2004.

[5] McKay Besl. A method for registration of 3-d shapes. 1992.

[6] Muller Bouxsein, Boyd. Guidelines for assessment of bone microstructure in rodent using micro-computed tomografy.

[7] H A Bruck, S R Mcneill, M A Sutton, and W H Peters Iii. Digital Image Correlation Using Newton-Raphson Method of Partial Differential Correction. pages 261–267, 1989.

[8] P-C Chang, K Liang, J C Lim, M-C Chung, and L-Y Chien. A comparison of the thresholding strategies of micro-CT for periodontal bone loss: a pilot study. *Dento maxillo facial radiology*, 42(2):66925194, January 2013.

[9] Dmitry Chetverikov, Dmitry Stepanov, and Pavel Krsek. Robust Euclidean alignment of 3D point sets: the trimmed iterative closest point algorithm. *Image and Vision Computing*, 23(3):299–309, March 2005.

[10] T C Chu, W F Ranson, M A Sutton, and W H Peters. Applications of Digital . Image-Correlation Techniques to Experimental Mechanics. (September):232–244, 1985.

[11] Stephen Corteen Cowin. *Bone mechanics handbook*, volume 1. CRC press Boca Raton, 2001.

[12] Ming Ding, Anders Odgaard, Carl Christian Danielsen, and Ivan Hvid. Mutual associations among microstructural, physical and mechanical properties of human cancellous bone. *The Journal of bone and joint surgery. British volume*, 84(6):900–7, August 2002.

[13] David Eberly and Geometric Tools. Fitting 3D Data with a Cylinder. pages 1–4, 2013.

[14] David Eberly and Geometric Tools. Least squares fitting of data. pages 1–10, 2013.

[15] D.W. Eggert, a. Lorusso, and R.B. Fisher. Estimating 3-D rigid body transformations: a comparison of four major algorithms. *Machine Vision and Applications*, 9(5-6):272–290, March 1997.

[16] Esposito. Il problema della co-registrazione di immagini biomedicali e sue applicazioni nell'ambito radiologico e diagnostico.

[17] Falco. Sviluppo di un protocollo per la caratterizzazione meccanica di tessuto osseo trabecolare finalizzata alla validazione di un modello numerico. *Tesi di laurea, Universit di Bologna*, 2012.

[18] S A Goldstein. The mechanical dependence properties of trabecular bone : on anatomic location and function. 1961.

[19] Yaacov Hel-or. Absolute Orientation from Uncertain Point Data : A Uni ed Approach 3 Uncertainty of The Primitives.

[20] Benedikt Helgason, Egon Perilli, Enrico Schileo, Fulvia Taddei, Sigurur Brynjólfsson, and Marco Viceconti. Mathematical relationships between bone density and mechanical properties: A literature review. *Clinical Biomechanics*, 23(2):135–146, 2008.

[21] Benedikt Helgason, Fulvia Taddei, Halldór Pálsson, Enrico Schileo, Luca Cristofolini, Marco Viceconti, and Sigurur Brynjólfsson. A modified method for assigning material properties to FE models of bones. *Medical Engineering & Physics*, 30(4):444–453, 2008.

[22] F. Hild and S. Roux. Digital Image Correlation: from Displacement Measurement to Identification of Elastic Properties - a Review. *Strain*, 42(2):69–80, May 2006.

[23] Iori. Micro-fem models based on micro-ct reconstructions for the in vitro characterization of the elastic properties of trabecular bone tissue. *Master Thesis, University of Bologna.*

[24] Max A. Viergever J.B.Antoine Maintz. *A survey of medical image registration.*

[25] David L Kopperdahl and Tony M Keaveny. Yield strain behavior of trabecular bone. *Journal of Biomechanics*, 31(7):601–608, 1998.

[26] A J Ladd, J H Kinney, D L Haupt, and S A Goldstein. Finite-element modeling of trabecular bone: comparison with mechanical testing and determination of tissue modulus. *Journal of orthopaedic research : official publication of the Orthopaedic Research Society*, 16(5):622–8, September 1998.

[27] Lionello. Messa a punto del metodo di correlazione d'immagine per applicazioni biomediche. *Tesi di laurea, Universit di Bologna.*

[28] Evgeny Lomonosov, Dmitry Chetverikov, and Anikó Ekárt. Pre-registration of arbitrarily oriented 3D surfaces using a genetic algorithm. *Pattern Recognition Letters*, 27(11):1201–1208, August 2006.

[29] S.R. McNeill, W.H. Peters, and M.A. Sutton. Estimation of stress intensity factor by digital image correlation. *Engineering Fracture Mechanics*, 28(1):101–112, 1987.

[30] Thomas L. Mueller, David Christen, Steve Sandercott, Steven K. Boyd, Bert van Rietbergen, Felix Eckstein, Eva-Maria Lochmüller, Ralph Müller, and G. Harry van Lenthe. Computational finite element bone mechanics accurately predicts mechanical competence in the human radius of an elderly population. *Bone*, 48(6):1232–1238, 2011.

[31] G. L. Niebur, J. C. Yuen, A. C. Hsia, and T. M. Keaveny. Convergence Behavior of High-Resolution Finite Element Models of Trabecular Bone. *Journal of Biomechanical Engineering*, 121(6):629, December 1999.

[32] Anders Odgaard, Jesper Kabel, Bert van Rietbergen, Michel Dalstra, and Rik Huiskes. Fabric and elastic principal directions of cancellous bone are closely related. *Journal of Biomechanics*, 30(5):487–495, 1997.

[33] Caroline Ohman, Massimiliano Baleani, Egon Perilli, Enrico Dall'Ara, Simone Tassani, Fabio Baruffaldi, and Marco Viceconti. Mechanical testing of cancellous bone from the femoral head: experimental errors due to off-axis measurements. *Journal of biomechanics*, 40(11):2426–33, January 2007.

[34] E. Perilli, M. Baleani, C. Öhman, R. Fognani, F. Baruffaldi, and M. Viceconti. Dependence of mechanical compressive strength on local variations in microarchitecture in cancellous bone of proximal human femur. *Journal of Biomechanics*, 41(2):438–446, 2008.

[35] E Perilli, F Baruffaldi, M Visentin, B Bordini, F Traina, a Cappello, and M Viceconti. MicroCT examination of human bone specimens: effects of polymethylmethacrylate embedding on structural parameters. *Journal of microscopy*, 225(Pt 2):192–200, February 2007.

[36] W. Pistoia, B. van Rietbergen, E.-M. Lochmüller, C.A. Lill, F. Eckstein, and P. Rüegsegger. Image-Based Micro-Finite-Element Modeling for Improved Distal Radius Strength Diagnosis. *Journal of Clinical Densitometry*, 7(2):153–160, 2004.

[37] Peter J. Rousseeuw. Least Median of Squares Regression. *Journal of the American Statistical Association*, 79(388):871, December 1984.

[38] M J Silva, T M Keaveny, and W C Hayes. Computed tomography-based finite element analysis predicts failure loads and fracture patterns for vertebral sections. *Journal of orthopaedic research : official publication of the Orthopaedic Research Society*, 16(3):300–8, May 1998.

[39] Bone Histomorphometry Standardization, A Michael Parfitt Chairman, Marc K Drezner, Francis H Glorieux, John A Kanis, Hartmut Malluche, Pierre J Meunier, Susan M Ott, and Robert R Recker. Bone Histomorphometry : Standardization. 2(6), 1987.

[40] Sutton. *Image correlation for shape motion and displacement.*

[41] Ardiyansyah Syahrom, Mohammed Rafiq Abdul Kadir, Jaafar Abdullah, and Andreas Öchsner. Mechanical and microarchitectural analyses

of cancellous bone through experiment and computer simulation. *Medical & biological engineering & computing*, 49(12):1393–403, December 2011.

[42] S. Tassani. Dottorato di ricerca " Evaluation of bone strength :microtomographic techniques". 2009.

[43] D Ulrich, B van Rietbergen, A Laib, and P Ruegsegger. The ability of three-dimensional structural indices to reflect mechanical aspects of trabecular bone. *Bone*, 25(1):55–60, 1999.

[44] G. Harry van Lenthe and Ralph Müller. Prediction of failure load using micro-finite element analysis models: Toward in vivo strength assessment. *Drug Discovery Today: Technologies*, 3(2):221–229, 2006.

[45] B. Van Rietbergen, A. Odgaard, J. Kabel, and R. Huiskes. Direct mechanics assessment of elastic symmetries and properties of trabecular bone architecture. *Journal of Biomechanics*, 29(12):1653–1657, 1996.

[46] B van Rietbergen, H Weinans, R Huiskes, and a Odgaard. A new method to determine trabecular bone elastic properties and loading using micromechanical finite-element models. *Journal of biomechanics*, 28(1):69–81, January 1995.

[47] E Verhulp, B.van Rietbergen, and R Huiskes. A three-dimensional digital image correlation technique for strain measurements in microstructures. *Journal of Biomechanics*, 37(9):1313–1320, 2004.

[48] E Verhulp, B van Rietbergen, and R Huiskes. Comparison of micro-level and continuum-level voxel models of the proximal femur. *Journal of biomechanics*, 39(16):2951–7, January 2006.

[49] Marco Viceconti, Mario Davinelli, Fulvia Taddei, and Angelo Cappello. Automatic generation of accurate subject-specific bone finite element models to be used in clinical studies. *Journal of Biomechanics*, 37(10):1597–1605, 2004.

[50] Wirtz. Critical evaluation of known bone material properties to realize anisotropic fe-simulation of the proximal femur. *Journal of biomechanics*, 33(10):1325–30, October 2000.

[51] Uwe Wolfram, Hans-Joachim Wilke, and Philippe K Zysset. Valid micro finite element models of vertebral trabecular bone can be obtained using tissue properties measured with nanoindentation under wet conditions. *Journal of biomechanics*, 43(9):1731–7, June 2010.

[52] Barbara Zitová and Jan Flusser. Image registration methods: a survey. *Image and Vision Computing*, 21(11):977–1000, 2003.

[53] Zuppante. Qualitative analysis of a microtomographic apparatus and measurement of the bone tissue density with reference to microgravity conditions. *Tesi di dottorato Universit di Padova*.